Lawrence Berkeley Laboratory
UNIVERSITY OF CALIFORNIA

Materials & Molecular
Research Division

TIME-RESOLVED SPECTROSCOPY USING SYNCHROTRON RADIATION

Erwin David Poliakoff
(Ph. D. thesis)

August 1979

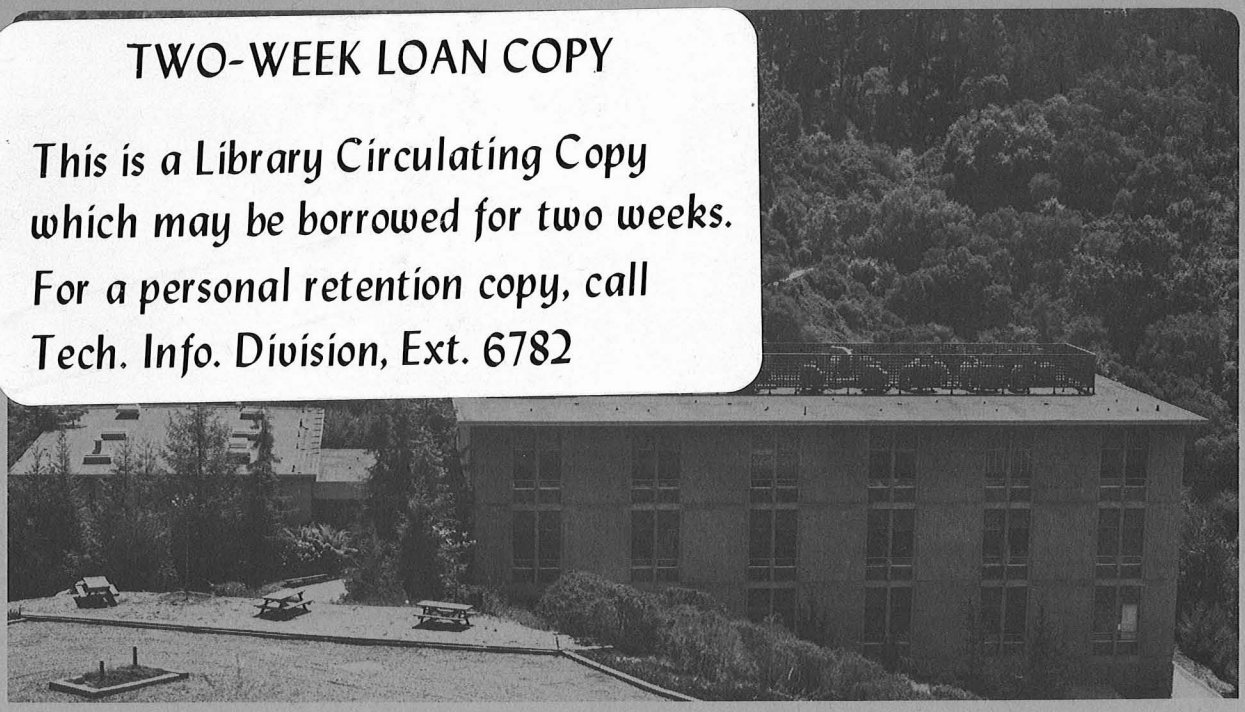

Prepared for the U. S. Department of Energy
under Contract W-7405-ENG-48

TIME-RESOLVED SPECTROSCOPY USING SYNCHROTRON RADIATION

Erwin David Poliakoff

Materials and Molecular Research Division
Lawrence Berkeley Laboratory

and

Department of Chemistry
University of California
Berkeley, CA 94720

Abstract

Work performed at the Stanford Synchrotron Radiation Laboratory (SSRL) is reported. The timing characteristics of the SPEAR beam (pulse width ≤ 0.4 nsec, pulse repetition period = 780 nsec) were exploited to determine dynamic behavior of atomic, molecular, excimeric, and photodissociative gas-phase species excited by vacuum-ultraviolet (VUV) radiation. Fast fluorescence timing measurements were done to determine excited-state lifetimes of Kr and Xe. Pressure-dependent timing studies on Xe gas at higher concentrations demonstrated some of the problems associated with previous kinetic modeling of the Xe_2 system. It was found that even qualitative agreement of observed Xe_2 lifetimes as a function of pressure required the assumption that the radiative lifetime was a strong function of internuclear separation. The radiative decays of chemically unstable fragments, $CN^*(B^2\Sigma^+)$ and $XeF^*(B^2\Sigma^+$ and $C^2\Pi_{3/2})$, were studied by pulsed photodissociation of stable parent compounds, ICN and XeF_2. When the polarization of the $CN^*(B^2\Sigma^+)$ fragment fluorescence was measured, it was found to be non-zero and strongly dependent on excitation wavelength. This polarization is

related to the symmetry of the photodissociative surface via a classical model, and the variations in the polarization with wavelength is attributed to symmetry and lifetime effects of a *predissociating* parent molecule. Despite the drawbacks of limited availability and low radiation flux, synchrotron radiation is definitely a useful spectroscopic tool for VUV studies of gas-phase systems.

Acknowledgements

There are many people who made this work possible, and I could not thank all of them adequately in a reasonable amount of space. (My inadequate attempt follows...)

The graduate students that I worked with provided a personal and professional environment which accentuated the successes and softened the disappointments. I particularly wish to thank Mike White, Dick Rosenberg, Steve Southworth, and Keith Jackson.

I've had the pleasure of working with three fine research directors in the course of my graduate career. Dave Shirley oversaw all of the work included in this thesis, and I thank him for the scientific insight he injects into all that he does. Eckart Matthias was a principal mover in this work, particularly at the inception of the project. His efforts are appreciated; working with him was its own reward. The past year has been spent largely on collaborative work with Dick Zare. One more inspirational influence ...

Academic endeavors depend on people maintaining and enjoying their personal fulfillment. My family, as well as close friends, Kevin Finney, Darcy Neal, Steve Nett, Barbara Rose, Nancy Maloney, John Winslow, Chris Becker, Bob Jones and others (let's keep this list reasonable) made this thesis possible for me.

I wish to acknowledge the everpresent assistance and friendship of Dennis Trevor, Jim Pollard, Dick Escobales, Warren Harnden, Karen Janes, and Wini Heppler.

This work was supported by the Division of Chemical Sciences, Office of Basic Energy Sciences, U. S. Department of Energy, under Contract No. W-7405-Eng-48.

Some of this work was performed at the Stanford Synchrotron Radiation Laboratory which is supported by the NSF Grant No. DMR 73-07692 A02, in cooperation with the Stanford Linear Accelerator Center.

Table of Contents

Table of Contents (continued)

Table of Contents (continued)

Chapter 1

Introduction

I. General

In recent years, the use of synchrotron radiation for spectroscopic studies has increased dramatically. The work reported in this thesis demonstrates the utility of the pulse structure at the Stanford Synchrotron Radiation Laboratory (SSRL) for the study of dynamic processes occurring in gas-phase systems. At the time that this experimental program started, there was a scarcity of synchrotron radiation experiments concerned with dynamic behavior. Thus, a diverse range of projects was carried out, probing the strengths and weaknesses of the synchrotron radiation source. This diversity is reflected in the contents which follow; to clarify the unifying aspects of the chapters, it is instructive to note where the common ground lies:

1) Atoms and simple molecules in the gas phase were studied at ambient temperature (~294°K).
2) Excitation energies were used in the range 4 eV ≤ hν ≤ 11.8 eV.
3) Signal detection involved fluorescence decay; i.e., experiments were of the form

$$A + h\nu \rightarrow B \rightarrow C + h\nu'$$

4) Fluorescence was observed as a function of time, the decay rates being the quantity of interest most often.

These points illustrate the nature of the work.

Firstly, atoms and simple molecules are of interest because they demonstrate most of the properties of interest to the physical chemist

with none of the perturbations found in condensed phases. For example, the excited-state lifetime is a sensitive probe of the electronic structure of these systems, and is directly comparable to state-of-the-art calculations. Secondly, the range of photon energies indicates that transitions involved valence electrons excited to unoccupied valence or Rydberg orbitals.

Fluorescence detection actually limited the scope of the work in some ways, especially in cases of fragmentation studies. Some of the fragmentation studies utilized the polarization properties of the synchrotron radiation to probe the dynamics of the fragmentation event. The angular distribution of photons fluoresced from excited-state fragments created via photodissociation are related to the symmetry of the dissociative surface. Thus, a measurement of the angular distribution of photons (or, equivalently, the fluorescence polarization) can yield the detailed nature of the dissociative surface(s). One obtains information of the type which is found in photofragment spectroscopy investigations.[1]

While offering advantages of experimental simplicity and yielding complementary information to photofragment spectroscopy, the polarization measurement is limited to generating data on surfaces with excited-state fragment asymptotes, an inherent limitation of the polarization technique (which is discussed in Chapter 5). Extensions of this technique, involving laser-induced fluorescence of the fragment, for example, could overcome this limitation[2] (though no measurements of this type have been done, to my knowledge).

The majority of the work, however, deals with the time-dependent radiative decay of excited states following pulsed photon excitation.

This provides information relative to photochemical and photophysical systems. In order to determine absolute rates of photochemical (or physical) processes involving an excited state, one must first know the rate of fluorescence (or equivalently, the radiative lifetime) of that state since radiative decay is a competitive process. For the simple case of non-reversible collisional quenching, Stern-Volmer kinetics[3] apply, and an example is found in Chapter 5, where a study of the collisional deactivation of the $CN^*(B^2\Sigma^+)$ state is discussed.

An additional advantage of synchrotron radiation (at SSRL) for such studies is that the excited states may be directly populated and the fluorescence decay can be directly monitored (not strictly true for photodissociation, as discussed in Chapter 5). This is in contrast to indirect techniques, such as pulsed electron-bombardment excitation[4] or modulated CW excitation with phase-shift detection.[5] A review of various methods of lifetime determinations is given by Imhof and Read[6] and related laser experiments are discussed by Yardley.[7]

The remainder of this thesis is partitioned as follows: a discussion of lifetimes is contained in Section II of this chapter. Properties of synchrotron radiation are reviewed in Section III. Chapters 2-4 concern radiative fluorescence decay. Chapter 2 reports atomic lifetime measurements; Chapter 3, Xe_2 radiative decay; Chapter 4, fragment radiative lifetimes following photodissociation; Chapter 5, polarization of fragment fluorescence to determine excited-state electronic symmetry (of dissociative surfaces); Chapter 6 discusses general conclusions briefly.

II. Lifetimes

If a system of atoms (or molecules) has N_k^0 atoms (or molecules) in an excited state, k, at time t_0, and decays to states, {i}, with rates $\{A_{ki}\}$, then the differential equation describing the population of state k as a function of time is

$$\frac{\partial N_k}{\partial t} = -N_k^0 \sum_i A_{ki}. \tag{1}$$

The solution to this equation is given simply by

$$N_k(t) = N_k^0 \exp[-t/\tau_k] \tag{2}$$

where

$$\tau_k \equiv [\sum_i A_{ki}]^{-1}. \tag{3}$$

One should note that the lifetime of level k, τ_k, is dependent on a sum of decay rates. Thus, if comparison of a theoretical value for τ_k and an experimental one disagree, the discrepancy is not easily traceable to a specific term. In many instances, however, the summation of Eq. (3) is restricted to a single term or a few terms. Then, τ_k becomes a more sensitive probe of the electronic structure of state k.

Now, the nature of the A_{ki}'s will be discussed for the illustrative case of an atom decaying from state k to state i via an electric-dipole transition. If both states k and i are non-degenerate,

$$A_{ki} = \frac{64\pi^4 \nu_{ki}^3}{3h} \left| \underset{\sim}{R}^{ki} \right|^2. \tag{4}$$

Here, ν_{ki} is the energy separation of states k and i in wavenumbers (cm^{-1}), h is Planck's constant, and

$$\underset{\sim}{R}^{ki} \equiv e\langle k|\sum_{\xi}\underset{\sim}{r}_{\xi}|i\rangle, \tag{5}$$

where e is the charge of the electron and $\underset{\sim}{r}_{\xi}$ is the position vector of the ξ^{th} electron coordinate. If states k and i are degenerate, Eq. (4) is still valid, though the quantity of interest is usually the total rate of depletion of a given magnetic sublevel, k_m, into all the magnetic sublevels, i_n, of state i. Now it is shown that this quantity is independent of magnetic sublevel, k_m.

$$A_{k_m i} = \frac{64\pi^4 \nu_{ki}^3}{3h} \sum_{n=-J_i}^{+J_i} |\langle kJ_k m|\sum_{\xi}\underset{\sim}{r}_{\xi}|iJ_i n\rangle|^2. \tag{6}$$

The quantity, $\sum_{\xi}\underset{\sim}{r}_{\xi}$, is the dipole operator and has components that transform as a spherical tensor, T_{vq}, of rank 1, i.e., v = 1. Thus, Eq. (6) is rewritten (dropping constant factors, using the Wigner-Eckart theorem)

$$A_{k_m i} \propto \sum_{q=-1}^{+1}\sum_{n=-J_i}^{+J_i} |\langle kJ_k m|T_{1q}|iJ_i n\rangle|^2$$

$$= |\langle kJ_k \| T_1 \| iJ_i\rangle|^2 \sum_{q=-1}^{+1}\sum_{n=-J_i}^{+J_i} |\langle J_k m|1J_i qn\rangle|^2, \tag{7}$$

where $\langle kJ_k \| T_1 \| iJ_i\rangle$ is a reduced matrix element and $\langle J_k m|1J_i qn\rangle$ is a Clebsch-Gordon coefficient.[8] A fundamental normalization property of the Clebsch-Gordon coefficients is

$$\sum_{q=-v}^{+v}\sum_{n=-J_i}^{J_i} |\langle J_k m|vJ_i qn\rangle|^2 = 1.$$

So, Eq. (7) is rewritten

$$A_{k_m i} \propto |\langle kJ_k \| T_l \| iJ_i \rangle|^2, \tag{8}$$

which is independent of the magnetic substate, k_m, that is decaying.

In hindsight, this result is obvious, since the independence on k_m only implies that the rate with which a substate decays is independent of its orientation in space. The same reasoning can be applied to molecular electronic decay and one finds that the lifetime is to be found independent of M_J (with J now referring to the rotational motion of the molecule). Additionally, A_{ki} is independent of J, as long as the rotational energy spacings are much smaller than the electronic energy difference of the transition. (Exceptions can be found, however, when particular J levels from one vibrational-electronic manifold are strongly mixed with rotational levels from a different electronic manifold.[2])

III. Synchrotron Radiation

The properties of synchrotron radiation have been reviewed extensively,[9-12] so only a brief account of the aspects pertinent to the contents of this thesis are discussed. When electrons are accelerated in a curved orbit with relativistic velocities, synchrotron radiation is produced with properties[9] very different than classical dipole, or simple antennae-generated radiation:

(1) The radiation has a continuous spectral distribution that extends from the IR to the VUV (X-ray, in some cases) range of the spectrum.

(2) The polarization of the radiation, P, usually exceeds that of classically produced dipole radiation. If s-type reflections[13] are used in the collection optics, it is possible that $P \geq 0.99$ for most wavelengths. The definition of P is

$$P \equiv \frac{I_{\parallel} - I_{\perp}}{I_{\parallel} + I_{\perp}} , \tag{9}$$

where $I_{\parallel}$ is the intensity with the $\underset{\sim}{\varepsilon}$-vector in the plane of the electron orbit, and $I_{\perp}$ is the intensity with ε-vector perpendicular to that plane. (Thus, as a design criterion for most beam lines that collect and monochromatize the radiation, vertical reflections are used whenever possible.)

(3) The radiation is nearly confined (referring to the angular spread) to the plane of the electron orbit.

(4) Some synchrotrons and electron storage rings produce radiation with pulse characteristics suited to timing experiments.

(5) The radiation is produced in an ultra-high vacuum environment; this is because the lifetime of a stored beam depends on the concentration of gas molecules. Collisions between electrons and gas molecules lower the intensity of the electron beam, and consequently, the synchrotron radiation.

The last feature is a drawback for gas-phase studies since the experimenter's chamber must be separated from the beam line by either a window material or a differential pumping section to prevent contamination of the electron storage ring. In the VUV and soft x-ray region of the spectrum, suitable window materials are frequently difficult or

impossible to obtain. Unfortunately, windowless, differentially-pumped beam lines are on the endangered species list.[14]

The work reported in this thesis was performed at the Stanford Synchrotron Radiation Laboratory (SSRL). Specifically, all experiments were performed at the 8° branch line of beam line I at SSRL. The features of this facility have been reviewed,[11] though some comments are in order. At this branch line, radiation is available in the range $4\ eV \leq h\nu \leq 36\ eV$ with a nominal photon flux of 10^{10} photons-sec^{-1}-Å^{-1} and polarization, P, greater than 97%.

One last general remark is that access to these facilities is not abundant. Some of the consequences of this are discussed in the thesis of Rosenberg.[15]

References (Chapter 1, Introduction)

1) See, for example, M. Kawasaki, S. J. Lee, and R. Bersohn, J. Chem. Phys. 63, 809 (1975).

2) This reference demonstrates the feasibility of such experiments W. M. Jackson, J. Chem. Phys. 61, 4177 (1974).

3) J. G. Calvert and J. Pitts, Photochemistry (John Wiley and Sons, Inc., New York, 1966).

4) A comparison of pulsed electron vs pulsed photon excitation can be found in M. Stock, R. E. Drullinger and M. M. Hessel, Chem. Phys. Lett. 45, 592 (1977).

5) See, for example, J. E. Hesser, J. Chem. Phys. 48, 2518 (1968) and references therein.

6) R. E. Imhof and F. H. Read, Rep. Prog. Phys. 40, 1 (1977).

7) "Dynamic Properties of Electronically Excited Molecules," by J. T. Yardley (Ch. 8 of Chemical and Biochemical Applications of Lasers, ed. C. B. Moore, Academic Press, 1974).

8) This discussion follows the reasoning of D. M. Brink and G. R. Satchler, Angular Momentum (Clarendon Press, Oxford, 1968), p. 58.

9) J. Schwinger, Phys. Rev. 75, 1912 (1949).

10) I. Lindau and H. Winick, Comments Atomic Mol. Phys. 6, 133 (1977).

11) S. Doniach, I. Lindau, W. E. Spicer, and H. Winick, J. Vac. Sci. Technol. 12, 1123 (1975).

12) M. L. Perlman, E. M. Rowe, and R. E. Watson, Physics Today, p. 30 (July, 1974).

13) S-type reflections are defined as those where the $\underset{\sim}{\varepsilon}$-vector of the incident beam is parallel to the reflecting surface. These reflections are polarization-enhancing.

14) An example of such a beam line is given in P. M. Guyon, C. Depautex, and G. Morel, Rev. Sci. Instrum. 47, 1347 (1976).

15) R. A. Rosenberg, Ph.D. Thesis, University of California, Berkeley (1979), unpublished (available as preprint from Lawrence Berkeley Laboratory, Berkeley, CA as #LBL-8948).

Chapter 2

Fluorescent Lifetimes of Atomic Kr and Xe

I. Introduction

Oscillator strengths for the $np^5(n+1)s^1$ levels in Xe and Kr have been the subject of investigations by several methods in the past, and the previously published results are not always mutually consistent (see Tables 1 and 2). Interest in obtaining accurate measurements of the atomic lifetimes has been increasing because the dimers have demonstrated laser potential. The lifetimes of these atomic states enter into the rate equations for formation of the dimers; thus accurate lifetime values are required to quantitatively describe the reaction kinetics.[1,2] In addition, the large spin-orbit splitting of the core hole state of heavier gases requires an alternate coupling scheme. Therefore, reliable experimental results are desirable to facilitate tests of various theoretical approaches.

In this chapter, the first values of five excited-state lifetimes in atomic krypton and xenon are reported as determined by resonance fluorescence decay. The results are compared with previous experimental values and with theory.

II. Experimental

The experiments were performed on the 8° beam line at SSRL. A detailed description of this facility was given elsewhere.[3] Briefly, 3.2 milliradians of radiation from the storage ring is subtended by a mirror and focused onto the grating of a 1-meter Seya-Namioka monochromator (UHV Design, GCA/McPherson). The dispersed light passes through an exit

slit (2 Å band pass) and enters the gas cell through a LiF window. The LiF window serves both to isolate the ultrahigh vacuum (1×10^{-10} torr) of the monochromator from the gas cell and to filter out higher-order light. The excitation energies are restricted, however, to wavelengths longer than 1050 Å because of the LiF cutoff. The light entering the gas cell is ≥ 97% plane-polarized and focused to a cross-section of approximately 1 mm × 3 mm.

The experimental apparatus and associated electronics are shown diagrammatically in Figure 1. An EMR 510-G photomultiplier (LiF window, CsI cathode), mounted perpendicular to both the propagation vector and the polarization vector, was used to detect the fluorescent radiation. The photomultiplier was placed approximately 2.5 cm and 1.0 cm from the interaction region for the Kr and Xe studies, respectively. The photomultiplier and associated electronics limited the time resolution of the experiments to ~1.8 nsec. There was no energy-selective device in the fluorescence channel because in atomic systems in the low pressure limit only resonance fluorescence occurs. The acceptance range for fluorescence was 1050-1850 Å due to the LiF-cutoff and the CsI response limit of the photomultiplier. Within this range only the spin-orbit doublet of the $4p^5 5s^1$ configuration in Kr could be excited, while in Xe the analogous levels plus several more states could be reached.

The data were recorded by a conventional single photon counting technique. The photomultiplier pulses were amplified and discriminated, then used as the start signals for the time-to-amplitude converter equipped with a single channel analyzer (Ortec model 467). The stop pulse was provided by a signal from an induction coil located in the

ring.* The data were accumulated in a multi-channel analyzer.

During these experiments, the electron beam current was between 12 mA and 18 mA, from which we expect a photon flux on the order of 10^{10}/sec. With sample pressure in the 10^{-6} range, the counting rate ranged from 1500 to 2500/sec., of which about one-third was true fluorescence events and two-thirds came from Rayleigh scattering of the incident light. Typical counting times were 60-90 min.

The gases were obtained from Airco Company, and were 99.995% pure. To maintain a fresh sample in the gas cell, the gas was continuously leaked into the sample chamber, which was pumped by a diffusion pump. The base pressure was 1×10^{-6} torr.

III. Results and Discussion

Typical decay curves are shown in Figure 2. Data analysis was done by means of a least-squares fitting routine in which the background was subtracted. The "prompt" peak with a maximum at time t = 0 (ca. channel 860) is due to the large number of Rayleigh scattering events, broadened by instrumental response, which is essentially Gaussian. This form of the response function was confirmed by measurements made off resonance, where Rayleigh scattering was present, but resonance fluorescence was not. The total observed resonance fluorescence decay curve is also broadened by the Gaussian "prompt" curve. Since the "prompt" curve is very narrow (FWHM = 1.8 ns), the true lifetime could be found by fitting at times far enough removed from t = 0, that the Gaussian had become negligible. The validity of this procedure was confirmed by analytical techniques. (See Appendix B of this chapter.)

*This results in a reversal of the time axis in Figure 2. It is necessary to avoid reset-time counting losses of the time-to-amplitude converter.

Lifetime measurements had to be carried out in the $10^{-5} - 10^{-6}$ torr pressure range to minimize the effects of resonance trapping. Even at these low pressures there is a finite probability for resonance scattering to occur before the fluorescence is detected. Such processes result in an apparent lifetime longer than the true one (see Appendix A). To obtain the true lifetime, the pressure dependences were measured and extrapolated to zero pressure. Figures 3 and 4 illustrate this procedure for the $^3P_1$ and $^1P_1$ states of Kr and Xe, as well as for the $5p^5(^2P_{3/2})5d$ J = 1 state in Xe for which the lifetime has not been measured before.

Because these are the first direct lifetime measurements on these systems by this method, we discuss briefly the sources of error. There are two non-negligible error sources: uncertainties in pressure measurements (leading to a typical error of ~2% in the extrapolated value of τ at t = 0), and statistical error (typically ~1%). Cumulative errors are given in Tables 1 and 2.

A comparison of the results with previous data and theoretical predictions are given in Table 1 for krypton and in Table 2 for xenon. The scatter as well as the large limits of error of the previous, less direct methods emphasize the need for direct resonance fluorescence lifetime measurements. An exception is the zero field level crossing measurement by Anderson[5] in Xe which we consider to be the most reliable set of earlier results. The results for the $^3P_1$ and $^1P_1$ levels in Xe are in good agreement with the values given by Anderson.[5] Comparing our experimental results with theoretical predictions, the nonrelativistic HF calculations of Dow and Knox[18] and of Kim, et al.[11] yield lifetimes that are too long, whereas the intermediate coupling scheme of Gruzdev[19,20] yields

values in very good agreement with experiment. A multiple configuration calculation by Gruzdev and Loginov (on Kr only) yields fairly good agreement.

The lifetime of the $5p^5(^2P_{3/2})5d$ J = 1 state at 1192 Å in Xe was determined in the same manner. The result $\tau = 1.40 \pm 0.07$ ns reflects the large oscillator strength of this transition. There are no theoretical predictions available for comparison. Calculations of Gruzdev and Loginov[20] however, yield a value of 1.87 ns for the lifetime of the analogous state in krypton, which confirms the trend observed in xenon.

In summary, this work reports the first lifetimes of atomic states excited by synchrotron radiation. No other method used for time-resolved spectroscopy can characterize the system as well as direct optical excitation. Our results demonstrate that the synchrotron radiation available at SPEAR, has both the necessary timing characteristic and sufficient intensity to study atomic lifetimes at very low pressures. These measurements yield accurate results for five levels in Kr and Xe, of which the $5p^5(^2P_{3/2})5d$ J = 1 state in Xe had not been previously reported. They also show the intermediate coupling approach to be the most useful for calculating these lifetimes.

APPENDIX A

Radiation Trapping

In order to explain the relative slopes of the lines in Figures 3 and 4, it is necessary to employ one of the theories on imprisonment of resonance radiation.[21-24] If τ_0 represents the true zero pressure lifetime, and τ the coherence time at some pressure, then it is predicted that

$$\tau = \frac{\tau_0}{1-x} \tag{A1}$$

where according to D'yakanov and Perel[24]

$$x = 1 - \frac{1}{\sqrt{\pi}} \int_{-\infty}^{\infty} \exp(-t^2)\exp(-k_0 L e^{-t^2})dt \tag{A2}$$

and according to Barrat[23]

$$x = 1 - \exp[-(\pi/6)^{\frac{1}{2}} k_0 L] \tag{A3}$$

and in both cases[21]

$$k_0 = \frac{2}{\Delta\nu_D}\left(\frac{\ell n 2}{\pi}\right)^{\frac{1}{2}} \frac{\lambda_0^2}{8\pi}\frac{N}{\tau_0} \tag{A4}$$

The quantity x represents the fractional absorption of resonance radiation by a layer of vapor of density N and thickness L; $1/k_0$ may be thought of as the minimum mean free path for absorption of resonance radiation of wavelength λ_0 and Doppler width $\Delta\nu_D$. For comparative purposes, the expression developed by Barrat will be used.*

---

*According to Nussbaum and Pipkin (see Ref. 25), both theories give equivalent results at sufficiently low values of the optical thickness, $k_0\ell$. For these measurements, $k_0\ell \sim 0.3$.

Substituting Eq. (3) into Eq. (1) and expanding the exponential, one obtains*

$$\tau = \tau_0(1 + (\pi/6)^{\frac{1}{2}} k_0 L + \ldots . \tag{A5}$$

or

$$\tau = \tau_0 + KLN \tag{A6}$$

where

$$K = (\pi/6)^{\frac{1}{2}} \frac{2}{\Delta\nu_D} \left(\frac{\ell n 2}{\pi}\right)^{\frac{1}{2}} \left(\frac{\lambda_0^2}{8\pi}\right) \frac{g_2}{g_1} .$$

Thus, a plot of τ - vs - N should yield to first order a straight line of slope KL.

Since in these experiments L was not well-defined, and to account for the different isotopes,[25] the only meaningful comparison is a ratio of the slopes of the lines for a given gas.

Equation (A6) predicts the slopes of the 5s[3/2]1 line and the 5s[1/2]1 line of Kr to be in a ratio of 1.2 : 1; the experimental result is 1.2 ± 0.2 : 1 for Xe; the predicted value of the slopes of the 5s[3/2]1 to 6s[1/2]1 to 5d[3/2]1 are 1.9 : 1.3 : 1.0, while experimentally the values are 1.9 ± 0.5 : 1.0 ± 0.3 : 1.0.

The experimental results are more than adequately explained by the theory, thus justifying the linear extrapolation used to obtain the zero pressure lifetime.

---

*Including terms only to first order introduces an error of $\sim(k_0\ell)^2$ or less than 10%. The data are insufficient to warrant inclusion of higher order terms.

APPENDIX B

Effect of System Response on Decay Curves

The work reported here involves determinations of extremely fast radiative decays. Since our detector with its associated electronics has a finite response time, it is necessary to consider the validity of the data in light of this experimental limitation. As was previously stated, the response function of the phototube was approximately gaussian in form with a FWHM of 1.8 nsec. This was determined via fluorescence timing measurements employing off-resonant excitation of the sample gas. Thus, only Rayleigh scattered photons were observed. Because the time scale of the Rayleigh scattering event is so short, the measurement is a direct determination of the system's response time. If a signal, I(t), is broadened by a systematic response, r(t-t'), then the observed signal, $I_{obs}(t)$, is given by

$$I_{obs}(t) = \int_{-\infty}^{\infty} I(t')\, r(t-t')dt' \tag{B1}$$

In our experiment, the signal is a simple one-exponential decay, starting at t = 0

$$I(t) = \begin{cases} 0, & t < 0 \\ \exp[-t/\tau], & t \geq 0 \end{cases} \tag{B2}$$

and we assume that the response function is given by a gaussian

$$r(t-t') = \exp[-(t-t')^2/2\sigma^2] \tag{B3}$$

where σ is related to the FWHM of the gaussian by

$$\sigma = \left(\frac{\ell n\ 2}{FWHM}\right)^{\frac{1}{2}} \tag{B4}$$

implying that $\sigma = 0.62\ \text{nsec}^{-\frac{1}{2}}$ for this work. Substituting (B2) and (B3) into (B1), then performing the integration, one obtains (neglecting constant factors)

$$I_{obs}(t) = [\exp(-t/\tau)] \cdot \{[\text{erf}[(t - \frac{\sigma^2}{\tau})(2\sigma^2)^{-\frac{1}{2}}]]+1\}\ , \tag{B5}$$

where

$$\text{erf}(x) \equiv \frac{2}{\sqrt{\pi}} \int_o^x e^{-u^2}\, du \tag{B6}$$

Because $\text{erf}[(t - \frac{\sigma^2}{\tau})(2\sigma^2)^{-\frac{1}{2}}]$ approaches a constant as $t \to \infty$, we conclude that $I_{obs}(t)$ approaches $I(t)$ as $t \to \infty$ (again neglecting constant factors). Quantitatively, for $t \geq 5$ nsec, $\sigma = .62\ \text{nsec}^{-\frac{1}{2}}$, and $\tau = 3.5$ nsec, we find (by expanding the error function) that the observed intensity traces out the real intensity to an accuracy exceeding one part in 10^8. Since all of the data were fitted for $t \geq 5$ nsec to eliminate contributions from Rayleigh scattered photons, the results quoted have not been significantly perturbed by instrumental response artifacts.

Table 1. Compilation of lifetimes and oscillator strengths for the two transitions $^3P_1 \rightarrow {}^1S_0$ and $^1P_1 \rightarrow {}^1S_0$ in Krypton.

$^3\tau$(ns)	^3f(1263Å)	$^1\tau$(ns)	^1f(1165Å)	method	authors	
4.14	0.166			resonance imprisonment	Turner[4]	(1965)
4.32 ± 0.33	0.159 ± 0.01	4.52 ± 0.35	0.135 ± 0.01	total absorption	Wilkinson[6]	(1965)
3.3 ± 0.8	0.21 ± 0.05	2.9 ± 0.7	0.21 ± 0.05	linear absorption	Chashchina and Shreider[9]	(1966)
3.37 ± 0.33	0.204 ± 0.020	3.32 ± 0.36	0.184 ± 0.020	optical line broadening	Vaughan[10]	(1968)
3.67 ± 0.12	0.187 ± 0.006	3.16 ± 0.15	0.193 ± 0.009	total absorption	Griffin and Hutcherson[12]	(1969)
4.0 ± 0.8	0.173 ± 0.035	3.5 ± 0.7	0.173 ± 0.035	electron energy loss	Geiger[13]	(1970)
		4.2 ± 0.4	0.142 ± 0.015	self-absorption	de Jongh and van Eck[15]	(1971)
3.18 ± 0.12	0.208 ± 0.006	3.11 ± 0.12	0.197 ± 0.006	resonance fluorescence	present work	
4.98	0.138	4.49	0.136	nonrel. Hartree-Fock	Dow and Knox[18]	(1966)
3.43	0.20	3.05	0.20	intermediate coupling calc.	Gruzdev[19]	(1967)
3.61	0.190	3.45	0.177	multiple conf. appr.	Gruzdev and Loginov[20]	(1975)

Table 2. Compilation of lifetimes and oscillator strengths for the two transitions $^3P_1 \rightarrow {}^1S_0$ and $^1P_1 \rightarrow {}^1S_0$ in Xenon.

$^3\tau$(ns)	^3f(1470Å)	$^1\tau$(ns)	^1f(1296Å)	method	authors
3.79 ± 0.12	0.256 ± 0.008	3.17 ± 0.19	0.238 ± 0.015	zero field level crossing	Anderson[5] (1965)
3.5 ± 0.6	0.28 ± 0.05	3.3 ± 0.7	0.23 ± 0.05	linear absorption	Chashchina and Shreider[8] (1965)
3.74 ± 0.25	0.260 ± 0.20	2.80 ± 0.20	0.270 ± 0.020	total absorption	Wilkinson[7] (1966)
		3.89 ± 0.10	0.194 ± 0.005	total absorption	Griffin and Hutcherson[12] (1969)
3.73 ± 0.75	0.260 ± 0.052	4.0 ± 0.8	0.190 ± 0.038	electron energy loss	Geiger[10] (1970)
3.57	0.272	3.99	0.189	low-energy electron impact	Lu[14] (1971)
4.6 ± 0.5	0.213 ± 0.020	4.2 ± 0.9	0.180 ± 0.040	resonance imprisonment	Wieme and Mortier[16] (1973)
5.31	0.183	4.47	0.169	low-energy electron impact	Delage and Carette[17] (1976)
3.46 ± 0.09	0.263 ± 0.007	3.44 ± 0.07	0.229 ± 0.007	resonance fluorescence	present work
5.00	0.194	5.13	0.147	nonrel. Hartree-Fock	Dow and Knox[18] (1966)
3.47	0.28	3.02	0.25	intermediate coupling calc.	Gruzdev[19] (1967)
4.58	0.212	3.99	0.189	nonrel. Hartree-Fock	Kim, et al.[11] (1968)

References for Chapter 2

1) G. Thornton, E. D. Poliakoff, E. Matthias, S.-T. Southworth, R. A. Rosenberg, M. G. White and D. A. Shirley, J. Chem. Phys. 71, 133 (1979).

2) R. Brodman and G. Zimmerer, J. Phys. B. 10, 3395 (1977).

3) H. Winick, VUV Radiation Physics, edited by E. E. Koch, et al. (Pergamon Viewpeg, 1974), p. 776; V. Rehn, et al., ibid. p. 780.

4) R. Turner, Phys. Rev. 140, A426 (1965).

5) D. Kent Andersson, Phys. Rev. 137, A21 (1965).

6) P. G. Wilkinson, J. Quant. Spectr. Rad. Transfer, 5, 503 (1965).

7) P. G. Wilkinson, J. Quant. Spectr. Rad. Transfer, 6, 823 (1966).

8) G. I. Chashchina and E. Ya. Shreider, Opt. Spectr. 20, 283 (1966).

9) G. I. Chashchina and E. Ya. Shreider, Opt. Spectr. 22, 284 (1967).

10) J. M. Vaughan, Phys. Rev. 166, 13 (1968).

11) Y. K. Kim, M. Inokuti, G. E. Chamberlain, and S. R. Mielezarek, Phys. Rev. Letters 21, 1146 (1968).

12) P. M. Griffin and J. W. Hutcherson, J. Opt. Soc. Am. 59, 1607 (1969).

13) J. Geiger, Phys. Letters 33A, 351 (1970).

14) K. T. Lu, Phys. Rev. A4, 579 (1971).

15) J. P. de Jough and J. van Eck, Physica 51, 104 (1971).

16) W. Wieme and P. Mortier, Physica, 65, 198 (1973).

17) A. Delage and J. D. Carette, Phys. Rev. A14, 1345 (1976).

18) J. D. Dow and R. S. Knox, Phys. Rev. 152, 50 (1966).

19) P. F. Gruzdev, Opt. Spectr. 22, 170 (1967).

20) P. F. Gruzdev and A. V. Loginov, Opt. Spectr. 38, 611 (1975).

21) A. C. E. Mitchell and M. W. Zemansky, Resonance Radiation and Excited Atoms, (Cambridge University Press, Cambridge, England, 1964).

22) T. Holstein, Phys. Rev. 72, 1212 (1947).

23) J. P. Barrat, J. Phys. Radium, 20, 541, 633, 657 (1959).

24) M. I. D'yakanov and V. I. Perel, Zh. Eksperim. i Teor. Fiz. 47, 1483 (1964) (Translation: Soviet Phys.-JETP 20, 997 (1965)).

25) Gilbert H. Nussbaum and Frances M. Pipkin, Phys. Rev. Letters, 19, 1089 (1967).

Figure Captions

Figure 1. Schematic representation of experimental apparatus.

Figure 2. Fluorescence decay curve of Kr.

Figure 3. Lifetime vs pressure for Kr.

- ● 5s[3/2]1
- ■ 5s[1/2]1

Figure 4. Lifetime vs pressure for Xe.

- ● 6s[3/2]1
- ■ 6s[1/2]1
- ▲ 5d[3/2]1

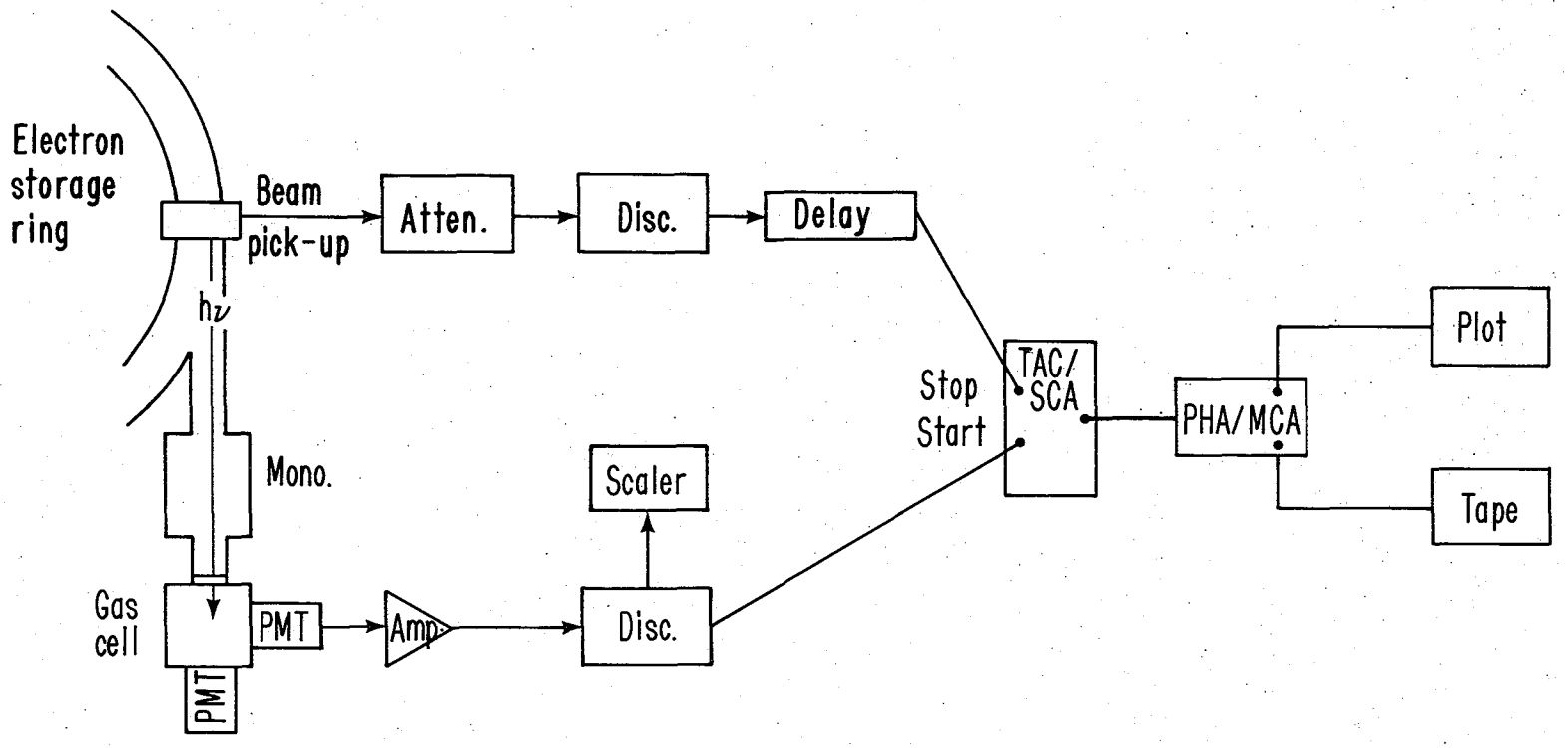

XBL-7612-4530

Figure 1

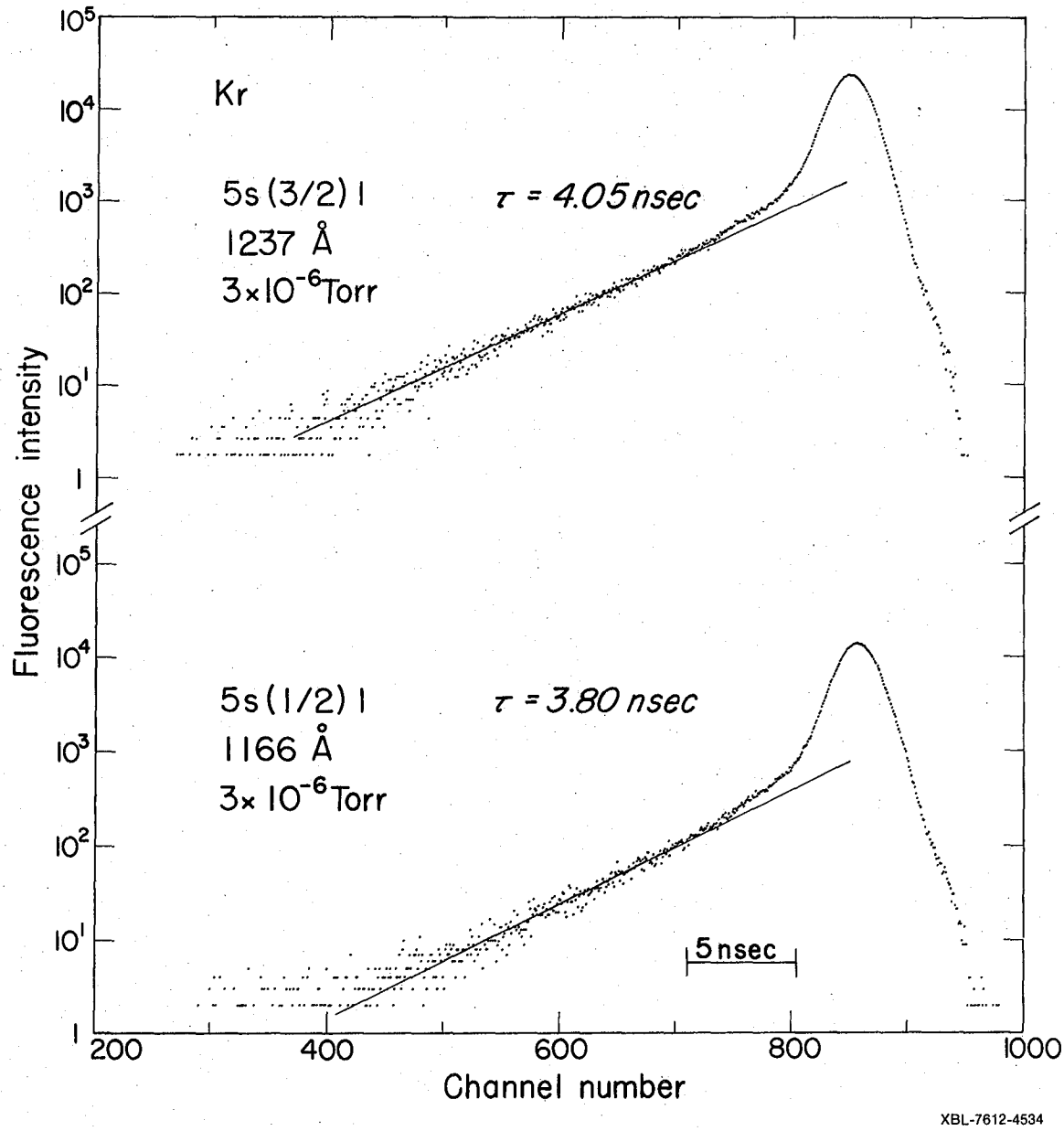
Kr
5s(3/2)1
τ = 4.05 nsec
1237 Å
3×10⁻⁶ Torr
5s(1/2)1
τ = 3.80 nsec
1166 Å
3× 10⁻⁶ Torr
5 nsec
Fluorescence intensity
Channel number
XBL-7612-4534

Figure 2

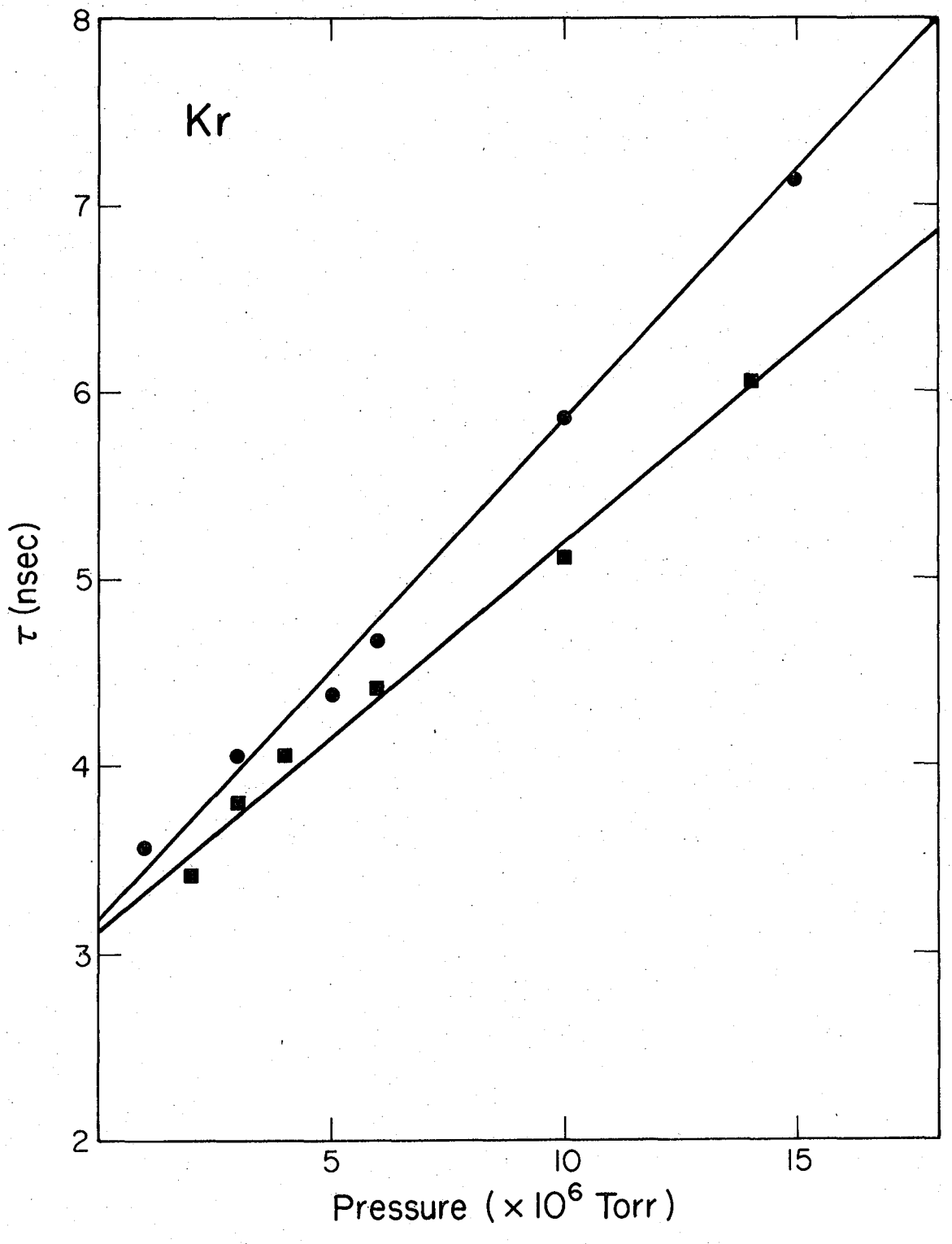

XBL-7612-4529

Figure 3

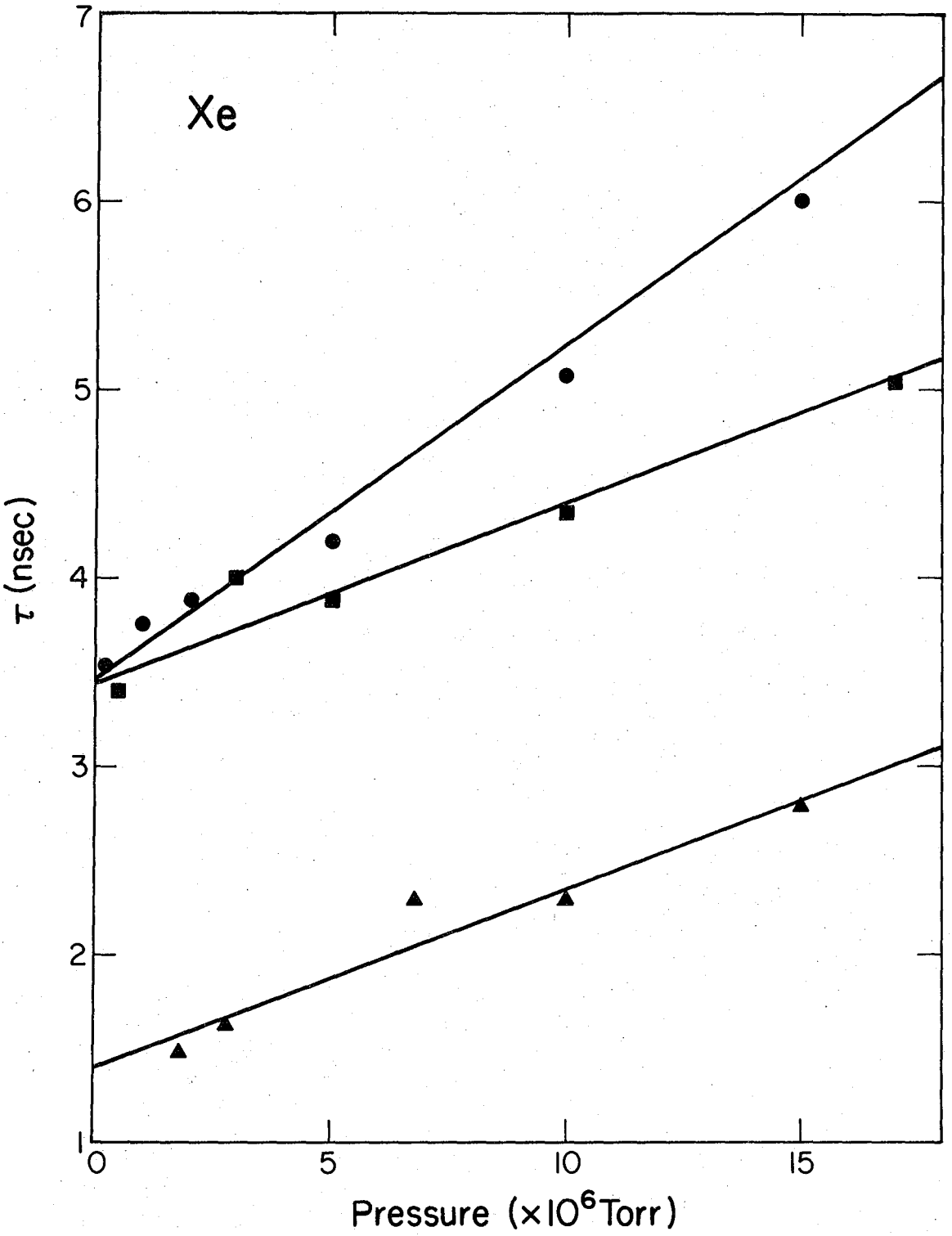

XBL-7612-4532

Figure 4

Chapter 3

Fluorescence Decay of the 0_u^+ and 1_u States of Xe_2

I. Introduction

There has been a great deal of recent interest in the use of electronically excited systems as ultraviolet lasing media.[1] For the continued development of these lasers, a detailed knowledge of the dynamics of the lasing transitions is desirable. In particular, the lasing efficiency is dictated by the population inversion, which depends strongly on the lifetime of the upper level.

The lasing transition in Xe_2, centered at 1700 Å, involves radiative decay of both the (vibrationally relaxed) 0_u^+ and 1_u excited states to the 0_g^+ ground state (see Fig. 1a).[2] Many attempts have been made to understand the salient dynamic processes of this system by the use of electron,[2-8] alpha-particle,[9] and optical[10-14] excitation at a number of sample pressures. The electron and alpha-particle excitation modes involve indirect excitation mechanisms; e.g., the formation of $Xe_2(0_u^+)$ via three-body collisions.[2] In the case of optical excitation the situation is rather confused since previous workers have used a variety of excitation energies. Most of the energies chosen would allow the formation of excited states in Xe_2 via creation of $Xe(^3P_{1,2})$ atomic states, as well as by population of the 0_u^+ and 1_u manifolds directly from the 0_g^+ ground state. This complication may well vitiate the conclusions that have been made about the 0_u^+ and 1_u lifetimes, even though photon excitation should in principle yield the least ambiguous results. In fact, previous work on Xe_2 has led to the proposal of several decay

mechanisms and has yielded a wide range of τ_{1_u} and $\tau_{0_u^+}$ values, summarized in Table 1.

In an attempt to clarify the situation we have used pulsed monochromatized synchrotron radiation to populate the upper vibrational levels of the 0_u^+ and 1_u electronic states of Xe_2 directly from the $X0_g^+$ ground state. Direct population of the lower levels is not possible because of their negligible Franck-Condon overlap with the bound portion of the $X0_g^+$ manifold. Three types of time-resolved experiments were employed. The first involved monitoring the monochromatized fluorescent decay from the upper (first continuum) and lower (second continuum) vibrational levels of the 0_u^+ and 1_u states. The second was concerned with the measurement of total fluorescent decay at various sample pressures. The same sample pressures were used in the third type of experiment with interference filters in the fluorescence channel, which were used to emphasize fluorescent decay from the upper, and the lower vibrational levels of $Xe_2(0_u^+,1_u)$. Section II describes the apparatus and the measurements that were carried out. In Section III the results obtained in the monochromatized (IIIA), total (IIIB) and filtered (IIIC) fluorescence experiments are described and compared with calculations based on a simple kinetic model. The overall conclusions of this work are presented in Section IV.

II. Experimental

The characteristic synchrotron pulse structure at the Stanford Synchrotron Radiation Laboratory (SSRL) (0.4 ns width, 780 ns repetition period) was utilized as a time base for time-resolved spectroscopy.[15] Monochromatized radiation (8.7 Å FWHM) from the 8° branch line at SSRL was used for excitation.

A schematic diagram of our apparatus is shown in Figure 2. Monochromatized radiation enters a bakeable UHV chamber before passing through a LiF window into a gas cell. Fluorescent radiation can then be detected below the cell. To ensure that no significant amounts of impurities were present in the sample, absorption spectra were measured using an optical photomultiplier (PMT) placed along the beam axis. A sodium salicylate film on the adjacent pyrex window served as a scintillator.

The monochromator experiment employed a highly polished, Pt-coated quartz toroidal mirror[16] to focus fluorescent radiation onto the entrance slit of a GCA/McPherson 218 monochromator (operated at 50 Å band pass). Because of the very low counting rates ($2s^{-1}$) encountered in the monochromatized fluorescence measurements, it was impractical to collect decay data at more than one pressure using this apparatus. However, pressure dependence of the non-monochromatized, total fluorescence decay was measured. In addition, broad-band interference filters were used, chosen to emphasize the two fluorescence continua separately: 1325 ± 92 Å, and 1710 ± 110 Å (Acton Research Corporation). (The 1325 Å filter was chosen because wings of transmission stressed the vibrationally unrelaxed levels.) In this arrangement both the filter and the PMT window could be placed within 1 cm of the interaction region,[15] resulting in typical counting rates of 1500 s^{-1}. In all experiments an EMR 510G photomultiplier tube was used to detect the fluorescence. This PMT has a uniform response over the wavelength range under study. Using Rayleigh (prompt) scattering the overall time resolution was found to be 1.6 ns (FWHM).

All studies were carried out at ambient temperature (294 K). The sample pressure of the 99.995% pure xenon was 68 torr in the monochromator experiment and 5, 11, 25, 65, and 125 torr in the total fluorescence and

filter experiments, as measured using a calibrated transducer (I.C. Transducers, Inc.). Under these conditions the partial pressure of Xe_2 varies about a mean of ≈0.001% of the total pressure.

III. Results and Discussion

A. Monochromatized Fluorescence

Absorption of monochromatized radiation by van der Waals' molecules in the ground state yields the upper excimer state(s). At the resolution used for this study (8.7 Å FWHM in excitation) it is possible to irradiate selectively below, at, or above the dissociation energy of a given excimer state. However, resolution in the fluorescence spectrum of fine structure within a vibronic manifold is not possible. Others[10,11] have found the fluorescence spectrum, recorded with resolution ≥20 Å FWHM, to have two broad bands centered at *ca.* 1510 Å and *ca.* 1700 Å. These are termed the "first continuum" and "second continuum", respectively. They are thought to arise from transitions from the top and bottom of the 0_u^+ and 1_u manifolds (see Fig. 1a). We qualitatively reproduced these spectra, though our excitation wavelength was 1508 Å and our fluorescent band pass was 50 Å FWHM (see Fig. 1b). By exciting at 1508 Å (>2 kT below the $^3P_2 - {}^1S_0$ atomic resonance at 1491 Å), we were able to avoid much of the complexity associated with atomic metastable production[10] and extract the relevant lifetimes reported below. Figure 3 shows time-resolved fluorescent decay curves taken at fluorescence wavelengths that emphasize the two continua separately.

A pseudo-potential calculation by Ermler, Lee, and Pitzer[18] predicts a change in 0_u^+ radiative lifetime from *ca.* 3 ns at the top of the manifold to *ca.* 5 ns at the bottom. The corresponding values for the 1_u

radiative lifetime are expect to be *ca.* 40 ns at the top, and *ca.* 160 ns at the bottom of the manifold. This variation in lifetimes arises for three reasons; firstly, a change in coupling from Hund's case (a) at short internuclear distance to case (c) coupling at large internuclear distance.[18a] Secondly, spin-orbit coupling mixes a $^1\Pi_u$ state into the 1_u manifold at large values of internuclear distance, which serves to increase the $1_u - 0_g^+$ transition moment. The third reason for the variation in radiative lifetime with internuclear distance is the well-known ν^3 dependence of dipole transition probability.

Only a single, short-lived (τ = 2.1 ± 0.1 ns) component is observed at the first continuum wavelength of 1514 ± 25 Å (Fig. 3a). The calculations of Ermler, Lee, and Pitzer[18] indicate that the 0_u^+ state will be preferentially populated on excitation (by a factor of 10 over 1_u production); hence it is likely that fluorescence at the first continuum arises mainly from the decay of the 0_u^+ state. Furthermore, at 68 torr the decay of upper vibrational levels of both states is strongly influenced by collisional effects. Very short lifetimes (<1.6 ns, our instrumental response) are therefore expected for both states, and it is unlikely that the relatively weak 1_u first continuum component would be resolved in our experiment.

Fluorescence at the second continuum energy yields two decay components (Fig. 3b; the shorter component is depicted more clearly on an expanded time scale in Fig. 3c). We assign these two components to decay of the lowest vibrational levels of the 0_u^+ manifold[19] (6.9 ± 0.3 ns) and of the 1_u level (112 ± 2 ns), respectively, in approximate agreement with other workers.[2]

All but the lowest vibrational levels of the 0_u^+ and 1_u manifolds can decay either radiatively or via collisions. The lifetime of either the 0_u^+ or 1_u state obtained at the first continuum is a composite of these two processes; i.e.,

$$\tau_1^{-1} = \tau_{r1}^{-1} + kP$$

where τ_{r1} is the radiative lifetime of the upper levels, k is the rate constant for collisional decay and P is the Xe pressure.

The lowest vibrational levels of the 0_u^+ and 1_u manifolds are populated collisionally from upper levels. Hence, in the high-pressure limit the derived lifetimes approach the true high-pressure radiative lifetimes at the second continuum energy. The rate equations governing this system are just those of two radioactive decay series decaying independently in cascade (assuming no intersystem crossing), with only the first of each species initially present. This problem was solved analytically by Bateman.[20] While it is completely straight-forward to apply the Bateman equation to a decay chain of any length, we shall for brevity consider the case of two consecutive decays for each manifold, to compare our 0_u^+ and 1_u lifetimes with those of Bonfield, et al.[21] The decay rate from the bottom of each electronic manifold, following a single-step collisionally-induced deactivation mechanism from the top of the manifold, is given by

$$\frac{dN_2}{dt} = C\left[e^{-t/\tau_{r2}} - e^{-(\tau_{r1}^{-1} + kP)t}\right]$$

where τ_{r2} is the lifetime in the second continuum; i.e., at the *bottom* of the manifold, τ_{r1} and kP are as defined above, and C is a constant.

The fluorescence intensity from the second continuum, dN_2/dt, rises through a maximum then decreases with time with a behavior approaching exponential decay in the limit $t \to \infty$. If we choose a reference time T well beyond the maximum intensity, and if the conditions $\tau_{r1}^{-1} + kP >> \tau_{r2}^{-1}, (\tau_{r1}^{-1} + kP)T >> 1$ are satisfied, then the characteristic time interval τ_2 over which dN_2/dt decreases by a factor of e will quite closely approximate the true decay time τ_{r2}. We may relate our measured value of τ_2 to τ_{r2} and $(\tau_{r1}^{-1} + kP)$ by the expression

$$e^{-T/\tau_{r2}} - e^{-(\tau_{r1}^{-1}+kP)T} = e\left[e^{-(T+\tau_2)/\tau_{r2}} - e^{-(\tau_{r1}^{-1}+kP)(T+\tau_2)}\right] \quad (1)$$

Bonfield, et al.,[21] working at $P_{Xe} \geq 500$ torr, found, at the second continuum, lifetimes of 4.8 ns (0_u^+) and 100 ns (1_u) and a feeding rate, $(\tau_{r1}^{-1} + kP)$, of 0.179 ns^{-1}. Using Eq. (1) these values suggest measured lifetimes τ_2 at 68 torr of *ca.* 8 ns (0_u^+) and 101 ns (1_u). The remaining discrepancy between our results and theirs probably arises from several factors. For example, at 68 torr a multi-level model is required to describe the decay kinetics, i.e., the two decay model is an oversimplification. In addition, the lifetime τ_{r2} may actually be pressure-dependent at high pressures, especially for the long (1_u) component.

It is pertinent at this point to compare our results with those of Dutuit, et al.,[14] who investigated the second continuum fluorescence of Xe_2 using the ACO storage ring. They also utilized a monochromator in the fluorescence channel, set at 1750 ± 20 Å and 1730 ± 20 Å. At their longest excitation wavelength (1493 Å) they observed a two-component decay, with the first lifetime increasing from 6.0 ns at 50 torr to 10.8 ns at 200 torr and the second being *ca.* 500-700 ns over the same pressure range. There is a large discrepancy between our respective

results for the long component. The origin of this discrepancy probably resides in the short (73 ns) repetition period of ACO, which in this case will give rise to a poorly determined background. Additionally, it could be due to the use of an excitation wavelength (1493 Å) which is within 2 kT of the Xe $^3P_2$ - Xe $^1S_0$ absorption line, though there is fair agreement with our results for the short component.

B. Total Fluorescence

In general, least-squares fitting of the total fluorescence data yielded a three-component exponential decay. The results of the data analysis are shown in Table 2. The reciprocals of the long and intermediate lifetime components are plotted against pressure in Figures 4 and 5. It is clear that they deviate from the Stern-Volmer type of behavior expected if the models used previously to describe the system were valid in this pressure regime.[11] Generally, these models have involved the radiative decay of the upper populated levels of the 0_u^+ and 1_u states (first continuum) as well as non-radiative decay to the lowest levels followed by radiative decay of these lower levels[11] (responsible for the second continuum). A more rigorous model is outlined below which allows for fluorescence from all vibrational levels in the 0_u^+ and 1_u manifolds, as well as for collisionally induced relaxation.

Excitation of Xe_2 at 1508 Å will populate vibrational levels of the 0_u^+ and 1_u states near the top of their manifolds (see Fig. 1a). Following excitation, these levels can decay either radiatively (to the $X0_g^+$ ground state of Xe_2) or via collisions to lower vibrational levels. Intersystem crossing between the 0_u^+ and 1_u states is possible. However, Keto et al.[17] found that the rate constants of intersystem crossing are

small (10^{-24} - 10^{-22} cm^3 ns^{-1}) and they were not included in our calculation.

The decay of each manifold was represented in our model by the following reactions:

$$Xe_2(0_g^+) + h\nu \longrightarrow Xe_2^i \; v = 50 \text{ (instantaneous)}$$

$$Xe_2^i \; v = 50 \xrightarrow{k_{50}} Xe_2(0_g^+) + h\nu$$

$$Xe + Xe_2^i \; v = 50 \xrightarrow{k'_{50}} Xe + Xe_2^i \; v = 49$$

$$Xe_2^i \; v = 49 \xrightarrow{k_{49}} Xe_2(0_g^+) + h\nu \qquad (2)$$

$$Xe + Xe_2^i \; v = 49 \xrightarrow{k'_{49}} Xe + Xe_2^i \; v = 48$$

$$\vdots \qquad\qquad \vdots$$

$$Xe_2^i \; v = 0 \xrightarrow{k_0} Xe_2(0_g^+) + h\nu$$

$$i = 0_u^+ \text{ or } 1_u$$

The radiative decay constant of the 0_u^+ manifold was varied linearly with v from $k_{50} = 0.3861\ ns^{-1}$ to $k_0 = 0.1859\ ns^{-1}$, the corresponding values for the 1_u state being $2.564 \times 10^{-2}\ ns^{-1}$ and $6.212 \times 10^{-3}\ ns^{-1}$. These reciprocal radiative lifetimes were taken from the pseudo-potential calculations of Ermler, Lee, and Pitzer.[18] They are values found at points on the 0_u^+ and 1_u potential curves, and Franck-Condon effects were not included in the calculation. The non-radiative decay constants were also varied linearly, from $k'_{50} = 4.4 \times 10^{-18}\ cm^3\ ns^{-1}$ to $k'_1 = 1.76 \times 10^{-19}\ cm^3\ ns^{-1}$. These values were used for both excited state manifolds; they were estimated from values found for the Hg_2 system.[22]

The differential equations pertaining to the reaction scheme (2) were integrated numerically using a computer program which has been described elsewhere.[23] When the calculated total fluorescent intensity is plotted as a function of time after excitation, one would expect the resulting decay curve to contain 50 components, one for each vibrational level involved in the calculation. However, it was found that this curve could be quite accurately described by only two effective decay components; i.e., by a curve of the form $A_1 e^{-\kappa_1 t} + A_2 e^{-\kappa_2 t}$. The variations of κ_1 and κ_2 for both the 0_u^+ and 1_u states are shown in Figures 6 and 7. This was found to be true for *both* the simulated 0_u^+ and 1_u decay schemes.

It seems clear that the long decay component (Fig. 4) is due to the fluorescent decay of the 1_u manifold, because its lifetime is considerably longer than that found for other components (both measured and calculated). The variation of this component with pressure (Fig. 4) is followed qualitatively by the calculated curve (Fig. 7) and it can be thought of as arising from the change in the population distribution of 1_u vibrational levels as a function of pressure and time after photoexcitation. The variation of the short component of the calculated 1_u decay (Fig. 6) can be ascribed to a decrease in non-radiative lifetime with increase in pressure (Stern-Volmer behavior). Similar effects are apparent in the calculated fluorescent decay of the 0_u^+ state (Fig. 6).

The behavior of both the intermediate and short lifetimes found experimentally (Table 2 and Fig. 5) are rather more difficult to rationalize. It seems likely that the intermediate lifetime represents a *measured average* of the calculated short 1_u and long 0_u^+ component (Fig. 6), the averaging being an artifact of the least squares fit. To

illustrate this point we compare, in Fig. 8, the experimental decay curve obtained at 65 torr (Fig. 8(a)), and the calculated 0_u^+ and 1_u decay curves for P_{Xe} = 65 torr (Fig. 8(b)). The calculated fluorescence decay from each manifold was summed, with equal weighting and adjusted to give the same peak height as the experimental curve. This was fitted to a *three* exponential decay, the resulting lifetimes being 157.7(5) ns, 4.78(1) ns, and 1.903(8) ns.

The short lifetime (Table 2) is assigned to the short component of the calculated 0_u^+ decay (Fig. 6). The variation of the experimental short lifetime with pressure (Table 2) is somewhat similar to that observed for both the intermediate and long lifetimes, although this measurement is subject to the most error because it lies near the limit of our timing capabilities (1.6 ns). The calculated short component of the 0_u^+ decay does not exhibit the marked increase in τ^{-1} at low pressures present in the experimental curve. This probably arises because of the relatively large Franck-Condon overlap between the vibrational levels at the top of the 0_u^+ and 1_u manifolds and the ground vibrational level of the 0_u^+ manifold.

Overall, the simple kinetic model used is in qualitative agreement with our measurements. However, our results at 5 and 120 torr, which should approximate the radiative lifetimes of the upper and lower levels respectively, indicate that the radiative lifetimes calculated by Ermler, Lee, and Pitzer[18] are somewhat too large. It should be noted, however, that Franck-Condon effects, which were not included by these authors,[18] may play a significant role; the favorable overlap between wavefunctions of the upper vibrational levels of the 0_u^+ manifold and the 0_g^+ ground state (mentioned previously) is one such example.

C. Filtered Fluorescence Measurements

As a further test of the 0_u^+ and 1_u fluorescent decay model, lifetime measurements were also made with broad-band interference filters in the fluorescence channel. These were chosen to emphasize fluorescence from the first and the second continuum. The decay curves obtained were again fitted to three components.

At pressures lower than 125 torr the $\tau_{1_u}^{-1}$ vs P_{Xe} curves obtained with and without a filter in the fluorescence channel, tend to diverge (Fig. 4). This illustrates the deviation from a high pressure limit where fluorescence from only the lowest levels of the 0_u^+ and 1_u manifolds are observed, because the filters effectively weight fluorescent decay from vibrational levels centered around their peak transmission. Some fluorescence from the lower levels is observed (at *ca.* 1700 Å) with the 1325 Å filter because the tail of its transmission function extends into the second continuum region.

Similar effects occur in the variation of intermediate reciprocal lifetime with pressure (Fig. 5), although because of the nature of this component the dispersion of the curves pertaining to measurements obtained with and without filters is expected to be more complex.

IV. Summary

In conclusion, we have removed some confusion regarding the decay dynamics of the 0_u^+ and 1_u states of Xe_2, and have made a consistent analysis of their fluorescent decay. To achieve this, an excitation wavelength >2 kT below the $^3P_2 - {}^1S_0$ absorption line was employed, thus avoiding formation of $Xe_2(0_u^+, 1_u)$ by three-body collisions. The study was strengthened by utilizing both a monochromator and interference

filters in the fluorescence channel. By utilizing the theoretical lifetime calculations[18] we were able to model qualitatively the fluorescent decay of the 0_u^+ and 1_u states of Xe_2. The decay dynamics can be summarized as follows:

(1) At $P_{Xe} \gtrsim 100$ torr, the 0_u^+ and 1_u states, populated in their upper vibrational levels, decay rapidly and only the lower level of each manifold fluoresces.

(2) At $P_{Xe} \lesssim 100$ torr the relaxation data of others[11] were interpreted previously simply on the basis of a two-state (1^{st} and 2^{nd} continuum) model; however, a detailed study of the fluorescent lifetimes indicates that the true situation is too complex for this model to be valid. Intermediate vibrational levels of the 0_u^+ and 1_u states participate in the kinetic scheme, giving rise to a measured three-component total fluorescent decay. All components exhibit a *decrease* in lifetime at $P_{Xe} \lesssim 20$ torr and each can be assigned to the composite decay of vibrational levels of the 0_u^+ and 1_u manifolds.

At very low pressures we expect, of course, to observe just the radiative decay of those vibronic levels which were populated by photoexcitation.

A more complete study, using a high degree of monochromatization in the fluorescence channel, is clearly required in order to elucidate further the decay dynamics of this system and improve on the model proposed. When much higher intensity pulsed synchrotron radiation sources become available, such a study may be feasible.

Table 1. Compilation of lifetime measurements of lasing manifolds of Xe_2 (e.s.d.'s in parentheses)

$\tau_{0_u^+}$(high v) (ns)	$\tau_{0_u^+}$(low v) (ns)	τ_{1_u} (ns)	τ (ns)[a]	Reference
	5.5(10)	96.5(50)		2
			50(20)	3
			130(20)	4
			2000(500)	5
	4(1)	16(2.5)		6[b]
			16(2)	7
2		60		12
		102(2)		9
	6.0	770		14[c]

a) Unspecified.

b) Observed 280ns decay and assigned it to a lifetime of a highly excited state.

c) At 50 Torr.

Table 2. Experimental values of $\tau_{0_u^+}$, $\tau_{0_u^+,1_u}$, and τ_{1_u} at various P_{Xe}, using 1325Å and 1710Å interference filters, as well as no filter. All data were collected using λ_{ex} = 1508Å and e.s.d.'s are shown in parentheses. It has been assumed that the short lifetime is due to decay of Xe_2 0_u^+, the intermediate lifetime is due to Xe_2 $0_u^+,1_u$, while the long lifetime is due to decay of Xe_2 1_u (see text).

P_{Xe}	$\tau_{0_u^+}$ (ns)			$\tau_{0_u^+,1_u}$ (ns)			τ_{1_u} (ns)		
(Torr)	no filter	1325Å filter	1710Å filter	no filter	1325Å filter	1710Å filter	no filter	1325Å filter	1710Å filter
5	1.73(2)	——	——	7.4(4)	——	6.4(8)	53.2(7)	——	75.2(2)
11	1.96(3)	1.44(5)	1.51(5)	13.6(5)	——	8.6(6)	61.5(8)	——	75.(1)
25	2.57(2)	1.86(1)	2.02(6)	17.0(2)	——	18.5(6)	120.11(8)	——	103.(1)
65	2.64(3)	2.21(3)	3.1(2)	8.3(2)	5.9(3)	10.9(7)	105.3(3)	78.2(9)	83.1(4)
125	2.15(11)	2.38(6)	——	6.7(2)	6.2(6)	——	107.5(2)	108.(1)	102.(1)

References for Chapter 3

1) C. K. Rhodes, IEEE J. Quant. Electron 10, 153 (1974).

2) J. W. Keto, R. E. Gleason, Jr., and G. K. Walters, Phys. Rev. Lett. 33, 1365 (1974).

3) A. W. Johnson and J. B. Gerardo, J. Chem. Phys. 59, 1738 (1973).

4) S. C. Wallace, R. T. Hodgson, and R. W. Dreyfus, Appl. Phys. Lett. 23, 22 (1973).

5) R. Boucique and P. Mortier, J. Phys. D3, 1905 (1970).

6) H. A. Koehler, L. J. Ferderber, D. L. Redhead, and P. J. Ebert, Phys. Rev. A9, 768 (1974).

7) D. J. Bradley, M. H. R. Hutchinson, and H. Koester, Opt. Commun. 7, 187 (1973).

8) P. K. Leichner, K. F. Palmer, J. D. Cook, and M. Thieneman, Phys. Rev. A13, 1787 (1976).

9) P. Millet, A. Birot, H. Brunet, J. Galy, B. Pons-Germain, and J. L. Teyssier, J. Chem. Phys. 69, 92 (1978).

10) E. H. Fink and F. J. Comes, Chem. Phys. Lett. 30, 267 (1975).

11) R. Brodmann and G. Zimmerer, J. Phys. B10, 3395 (1977).

12) M. Ghelfenstein, R. Lopez-Delgado, and H. Szwarc, Chem. Phys. Lett. 49, 312 (1977).

13) M. Ghelfenstein, H. Szwarc, and R. Lopez-Delgado, Chem. Phys. Lett. 52, 236 (1977).

14) O. Dutuit, R. A. Gutchek, and J. LeCalvé, Chem. Phys. Lett. 58, 66 (1978). (We thank R. A. Gutchek for communicating a manuscript of the above prior to publication.)

15) For details see: E. Matthias, R. A. Rosenberg, E. D. Poliakoff, M. G. White, S.-T. Lee, and D. A. Shirley, Chem. Phys. Lett. 52, 239 (1977).

16) It is a pleasure to acknowledge Dr. Victor Rehn who designed the focusing mirror.

17) J. W. Keto, R. E. Gleason, Jr., T. D. Bonfield, G. K. Walters, and F. K. Soley, Chem. Phys. Lett. 42, 125 (1976).

18) W. C. Ermler, Y. S. Lee, K. S. Pitzer, and N. W. Winter, J. Chem. Phys. 69, 976 (1978).

18(a)) R. S. Mulliken, J. Chem. Phys. 52, 5170 (1970).

19) Calculations by Dutuit (personal communication) suggest that a small contribution to fluorescence at 1690 Å may arise from radiative decay of upper 0_u^+ vibrational levels.

20) H. Bateman, Proc. Cambridge Phil. Soc. 15, 423 (1910).

21) T. D. Bonfield, F. H. K. Rambow, G. K. Walters, M. V. McCusker, D. C. Lorents, and R. A. Gutchek, Stanford Synchrotron Radiation Laboratory Users Group Meeting, 1978 (SSRL Report No. 78/09), Stanford University, Stanford, CA 94305.

22) M. Stock, E. W. Smith, R. E. Drullinger, and M. M. Hessel, J. Chem. Phys. 68, 4167 (1978).

23) G. Z. Whitten, "Rate Constant Evaluations Using a New Computer Modeling Scheme", paper presented at the 167th National Meeting of the American Chemical Society, Spring 1974.

Figure Captions

Figure 1. (a) Potential curves for the relevant electronic levels in Xe_2 after Fink and Comes.[10]

(b) Fluorescence spectrum of Xe_2.

Figure 2. Schematic diagram of the monochromatized fluorescence apparatus.

Figure 3. Decay curves following excitation of Xe_2 at 1508 Å; (a) in the first continuum; (b) and (c) in the second continuum. In (c) the time scale is expanded to show the 0_u^+ lifetime.

Figure 4. $10^3 \times \tau_{1_u}^{-1}$ (ns^{-1}) vs P_{Xe} (torr), with values of τ_{1_u} taken from Table 2. (The lines connecting the data points were included for clarity.)

Figure 5. $10^2 \times \tau_{0_u^+,1_u}$ (ns^{-1}) vs P_{Xe} (torr), with values of $\tau_{0_u^+,1_u}$ taken from Table 2.

Figure 6. Calculated fluorescent decay of the 0_u^+ manifold both short and long, and the short component of the 1_u manifold as a function of Xe pressure.

Figure 7. Calculated fluorescent decay of the long component of the 1_u manifold as a function of Xe pressure.

Figure 8. Experimental decay curve obtained at 65 torr (a), and calculated decay of the 0_u^+ and 1_u manifolds at P_{Xe} = 65 torr (b). The calculated curve was scaled to give the same peak height as the experimental curve.

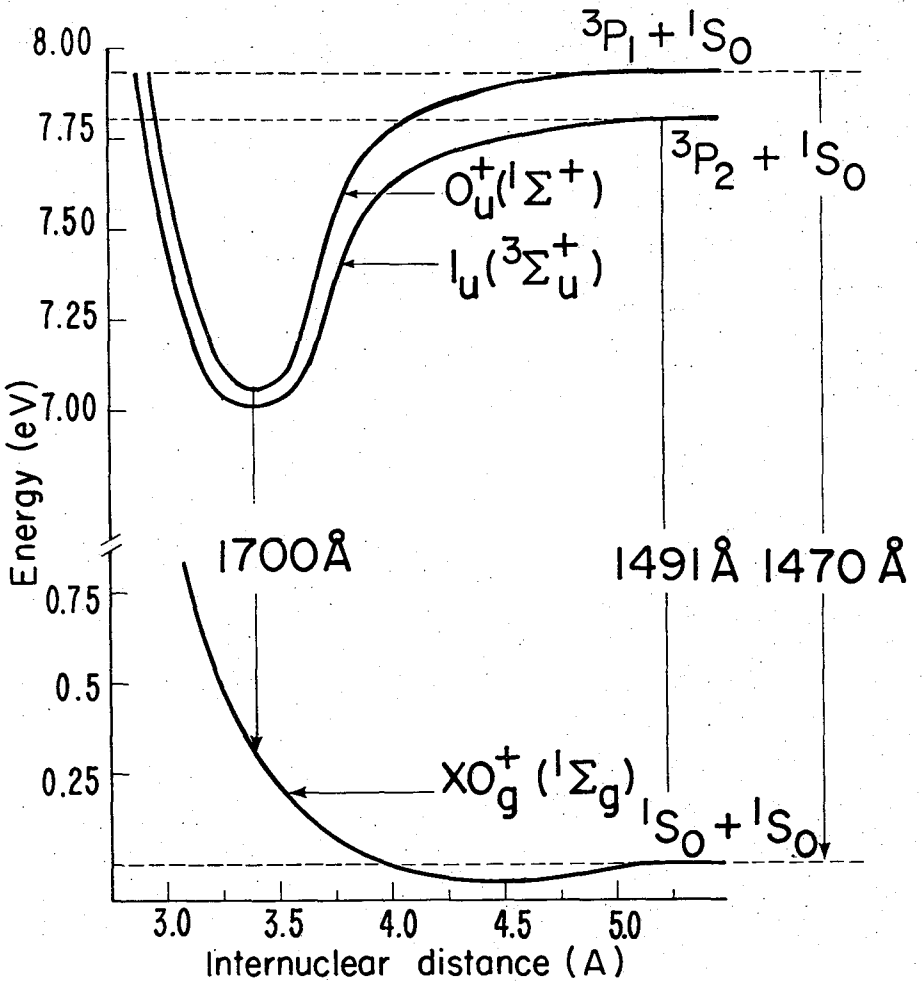

(a)

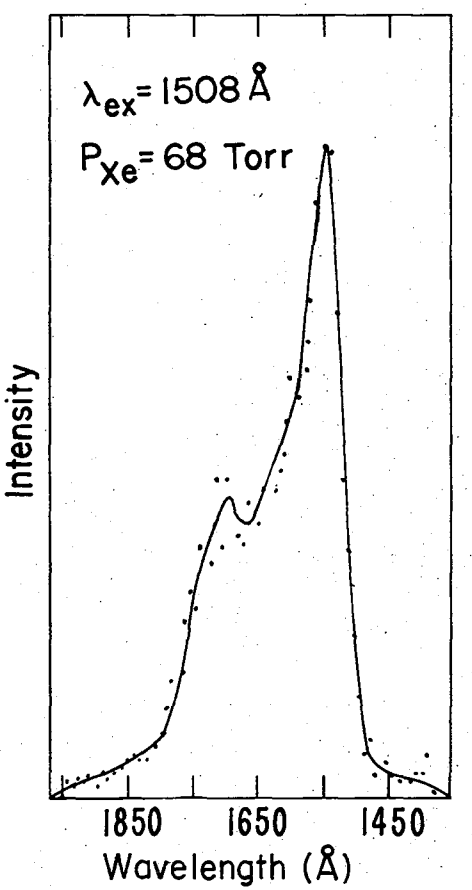

(b)

Figure 1

XBL 784-8217

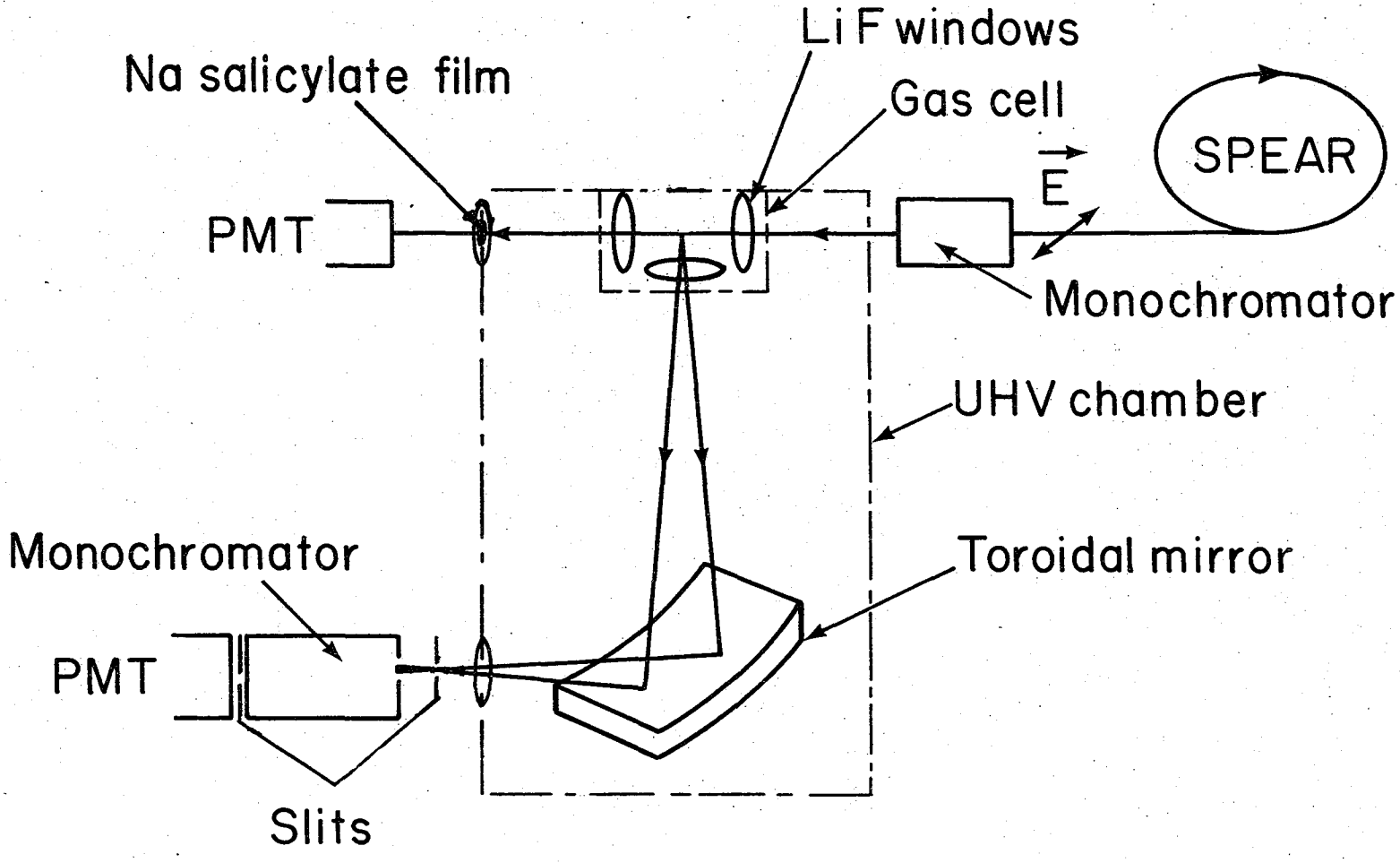
Na salicylate film
LiF windows
Gas cell
SPEAR
E
PMT
Monochromator
UHV chamber
Monochromator
Toroidal mirror
PMT
Slits
XBL 788-1651

Figure 2

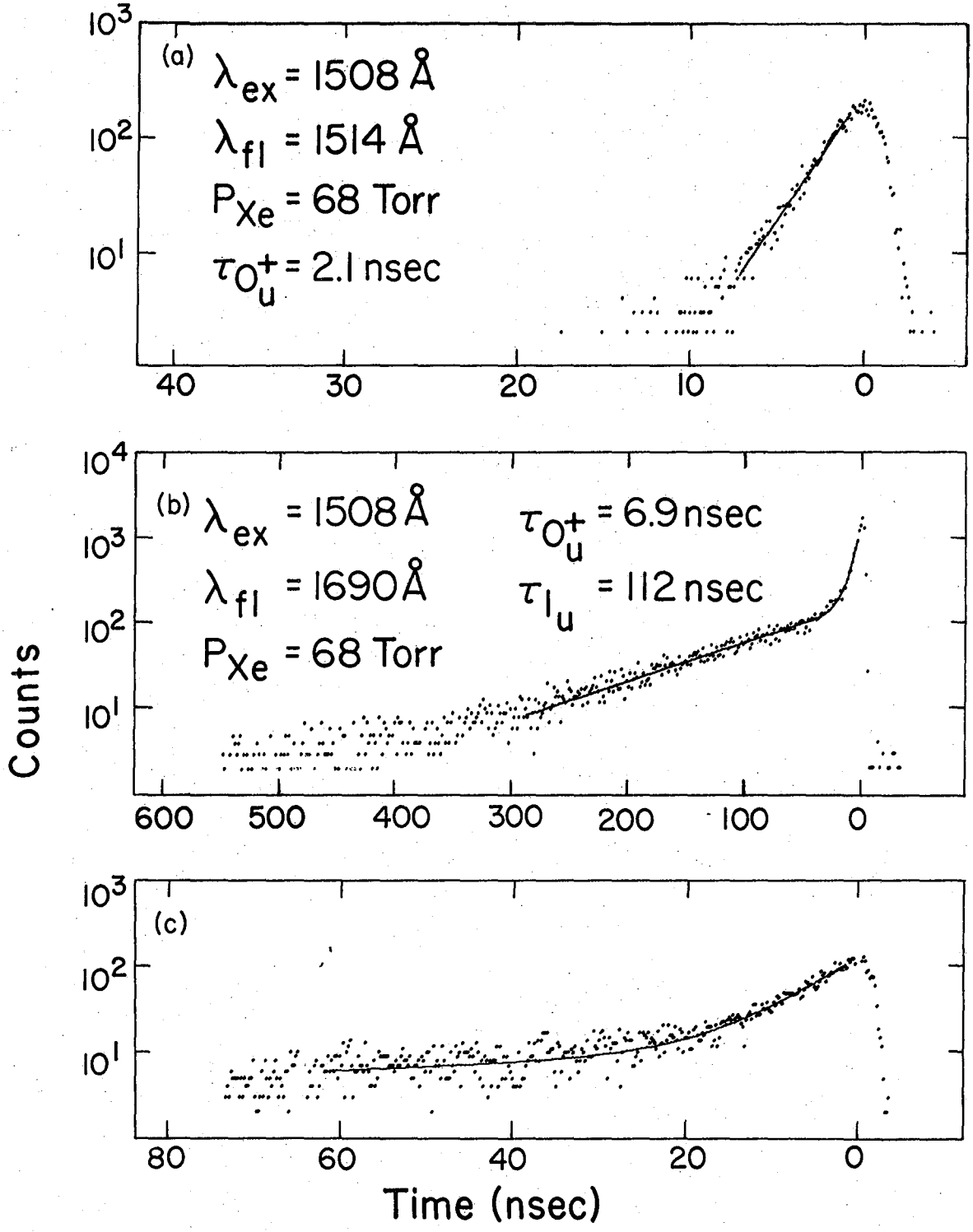

XBL 783-7888

Figure 3

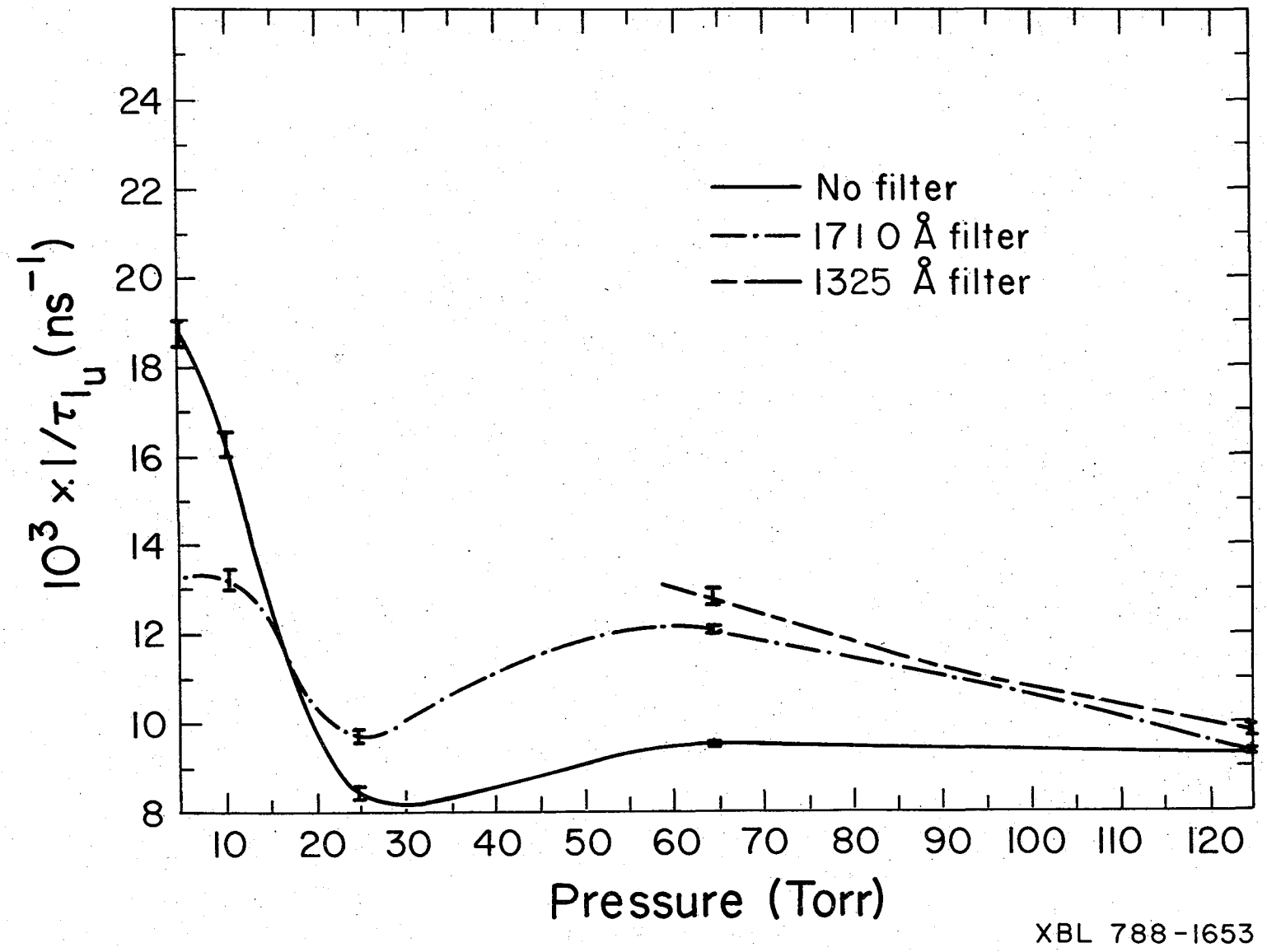

XBL 788-1653

Figure 4

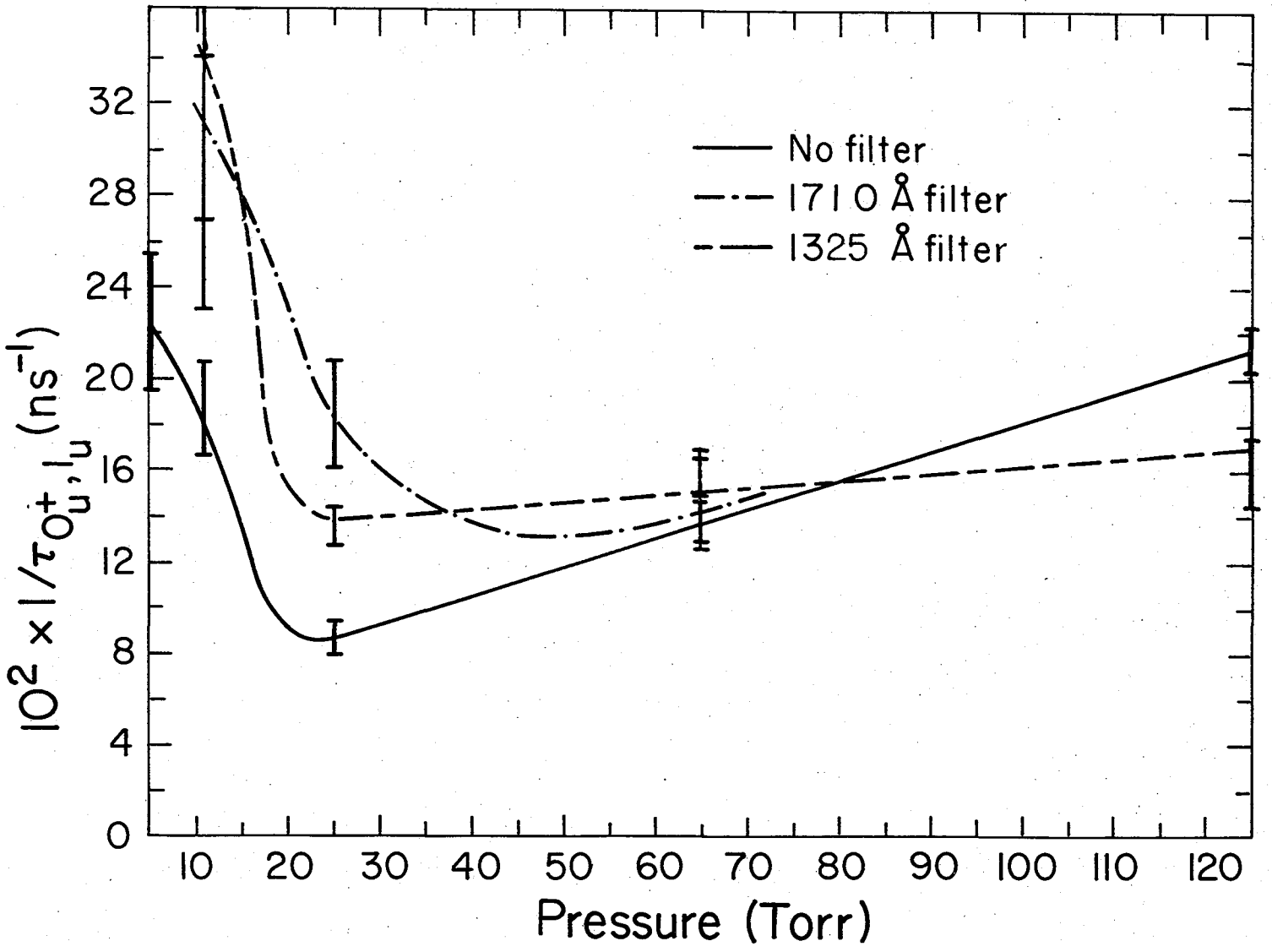

XBL 788-1652

Figure 5

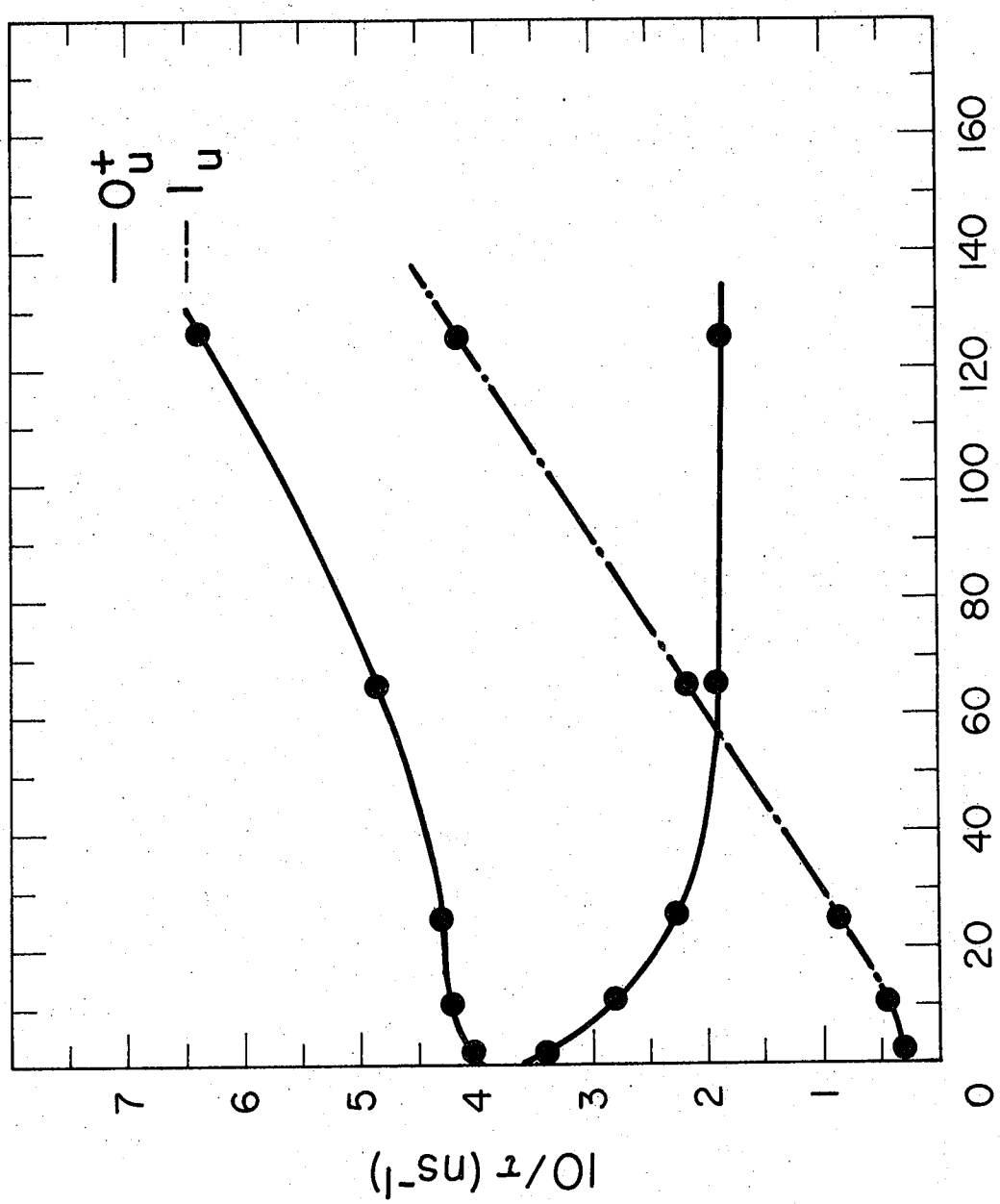

XBL789-2270

Figure 6

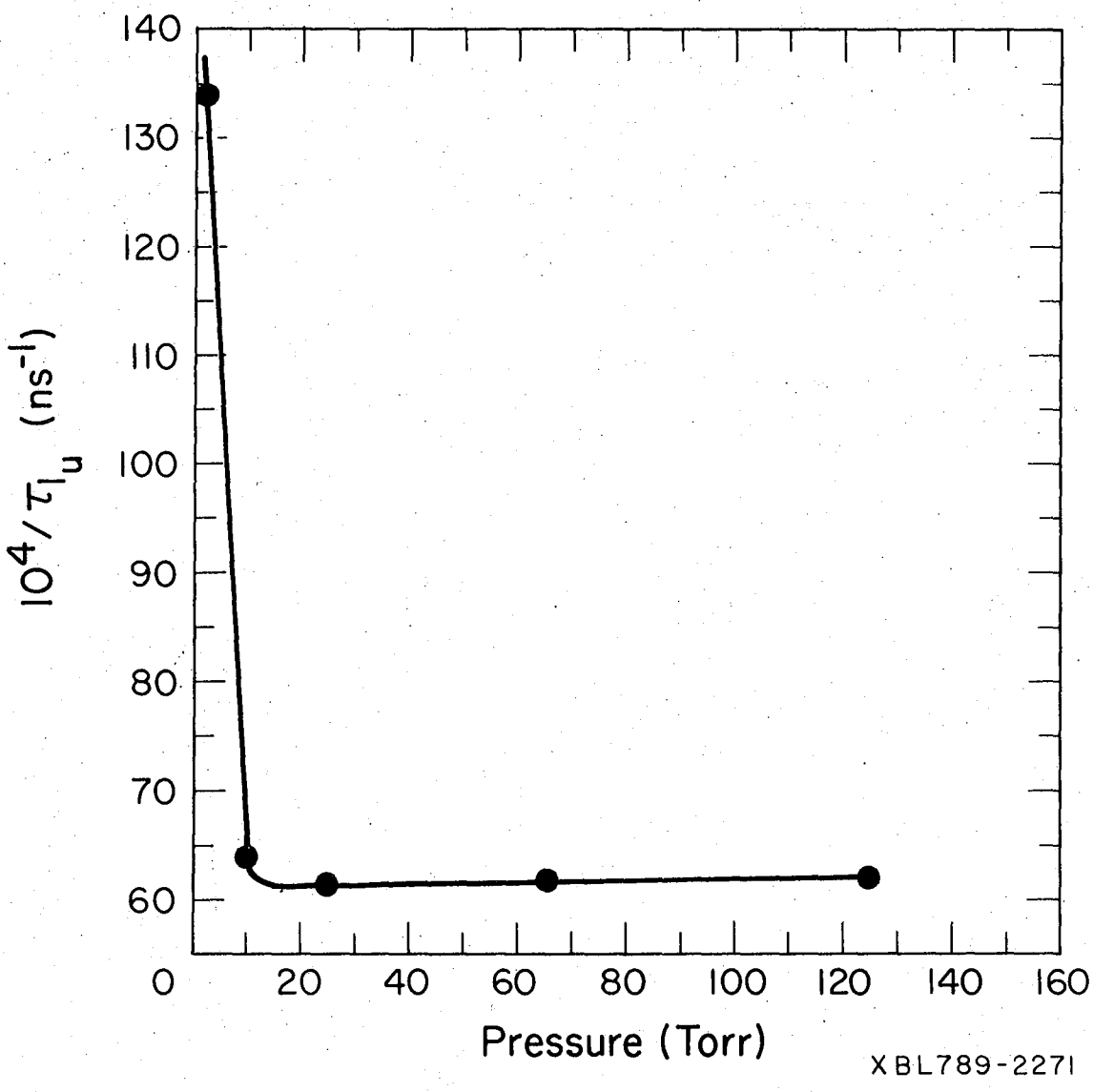
140
130
120
110
100
90
80
70
60
0
20
40
60
80
100
120
140
160
$10^4/\tau_{1_u}$ (ns^{-1})
Pressure (Torr)
XBL789-2271

Figure 7

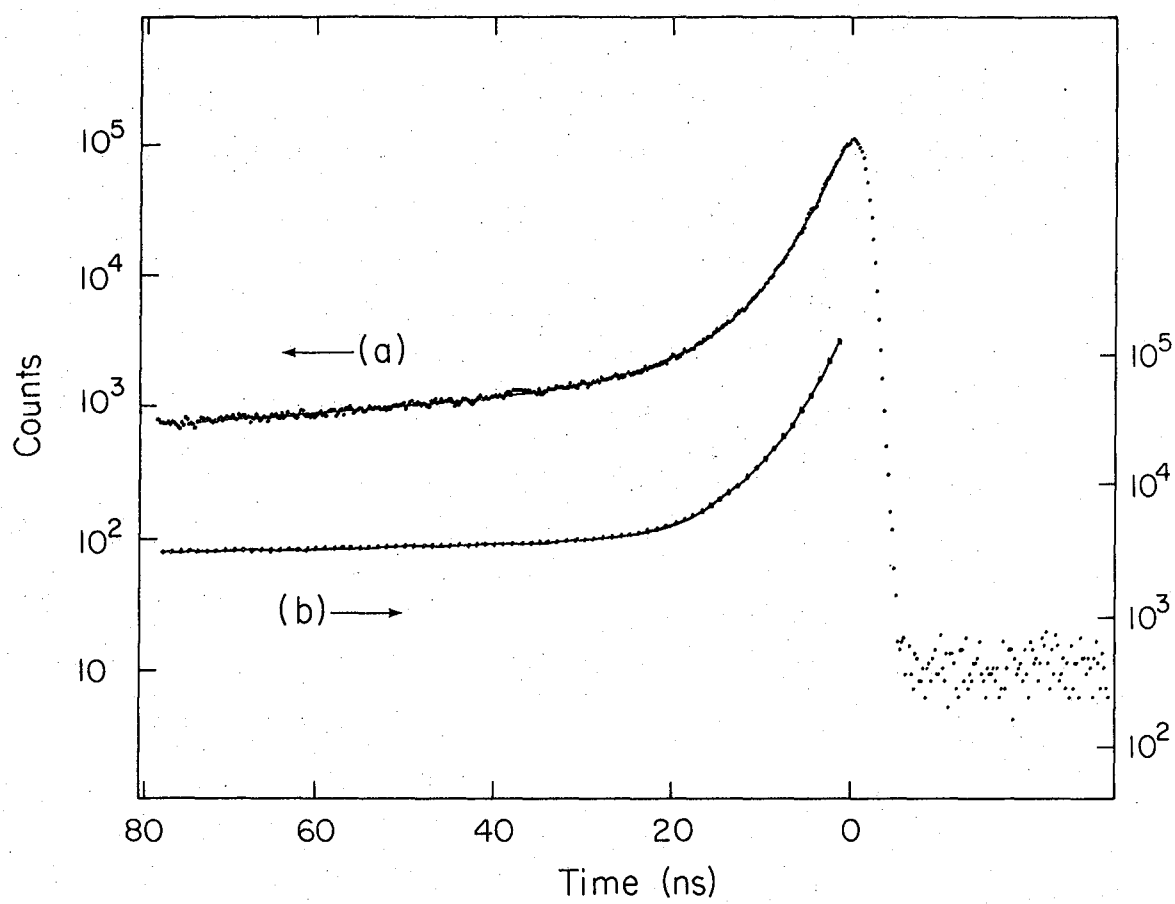

XBL 791-282

Figure 8

Chapter 4

Decay Dynamics of the $CN^*(B^2\Sigma^+)$ and $XeF^*(B^2\Sigma^+$ and $C^2\Pi_{3/2})$ States

I. Introduction

The radiative lifetimes of $CN^*(B^2\Sigma^+)$ and $XeF^*(B^2\Sigma^+$ and $C^2\Pi)$ have been the subjects of intense study. $CN(B \rightarrow X)$ transitions are observed in many astrophysical systems,[1a,b] and calculations of CN radical concentrations are dependent on accurate values for the strength of this transition. In addition, there have been many determinations of the $CN^*(B^2\Sigma^+)$ lifetime, yielding different values. Lifetime measurements on the $XeF^*(B^2\Sigma^+)$ state are motivated by two reasons. Firstly, the $XeF(B \rightarrow X)$ transitions contain several lasing lines, and the lasing gain is dependent upon the lifetime of the upper level. Secondly, the electronic structure of XeF has been a topic of current interest due to its relatively deep ground-state potential well.[2,3] The radiative lifetimes of excited states of XeF serve as stringent tests of theoretical wavefunctions used to compute the electronic structure of this radical.

Synchrotron radiation can be useful for the study of radiative decay following photodissociation. In particular, the pulse structure at SSRL allows one to follow the radiative decay on a nanosecond time scale. Recent studies on atomic,[4a-c] molecular,[5-7] and solid-state[8] systems have exploited the timing characteristics of synchrotron radiation[9] to study dynamic processes in excited states. One can also photodissociate a molecule using a synchrotron radiation pulse, produce electronically excited fragments, and study the radiative decay of the fragments. This is the nature of the work reported here, where excited

CN and XeF radicals were produced via the photodissociation of ICN and XeF_2, respectively.

Section II contains a description of the experiment; Section III discusses the data reduction and states the results. Straightforward kinetic modeling of the data is presented in Section IV. Section V contains conclusions of this work.

II. Experimental

The experimental setup has been described in a previous publication,[4a] so only a brief description is given here. A schematic diagram of the experimental arrangement is shown in Figure 1. Radiation at the Stanford Synchrotron Radiation Laboratory (SSRL) is pulsed with a 0.4 nsec pulse width and a 780 nsec repetition period. On the 8° branch line of beam line I, where this work was performed, photons with 4 eV $\leq h\nu \leq$ 36 eV are transmitted. A LiF window separated our chamber from the ultrahigh vacuum of the beam line optics, limiting our usable photon energy range to 4 eV $\leq h\nu \leq$ 11.8 eV. The wavelength bandwidth of the excitation radiation was 2.5 Å, providing a nominal photon flux of 10^{10} photons/sec.

Pressure measurement was done using a capacitance manometer (MKS #315 BHS-10) while the samples were in a flow system. In the case of the XeF_2 sample, the pressure measurement was not absolute because a conductance-limiting valve was placed between the capacitance manometer and the interaction volume. Thus, collisional quenching rates could not be determined absolutely although the intercepts from the extrapolation yielded reliable zero-pressure radiative lifetimes.

The ICN sample (≥99.5% pure) was obtained from Eastman Kodak and was used without further purification. ICN sample pressure was varied between 4.7×10^{-3} torr and 0.486 torr.

The XeF_2 sample was ≥99.9% pure for the volatile components. Our measurements used XeF_2 pressures between 1.75×10^{-2} and 1.21 torr. The fluorescence detection photomultiplier tube (RCA C31000 M) was placed perpendicular to both the propagation vector and the $\underset{\sim}{\varepsilon}$ vector of the exciting radiation.

A fluorescence excitation spectrum of ICN was recorded at a sample pressure of 8×10^{-3} torr. The fluorescence photons were time-gated such that only photons arriving within 60 nsec of the excitation pulse were counted. This was done to ensure that the excitation spectrum would not contain significant contributions from the $A^2\pi$ system, which is much longer-lived ($\tau_{CN^*(A^2\pi)} \geq 6$ μsec)[11] than the $B^2\Sigma^+$ state of CN^*.

Fluorescence decay curves were taken at the following excitation wavelengths: 1698 Å, 1575 Å, 1480 Å, and 1402 Å. A discussion of the timing electronics is contained in Ref. 4. The present measurements employed an interference filter (Microcoatings, Inc., #3850 BBC, peak transmission at 3850 Å, FWHM = 200 Å) to pass only the $CN(B \rightarrow X)$ emissions.[1b] At each wavelength, decay curves were obtained at four sample pressures to extrapolate out collisional effects.

For XeF_2, the excitation wavelength was set at 1690 Å, exceeding thresholds for $XeF^*(B^2\Sigma^+)$ and $XeF^*(C^2\Pi_{3/2})$ production.

All experiments were carried out at ambient temperature, ~294 K.

III. Results

A. ICN

The fluorescence excitation spectrum is shown in Figure 2. Spectral assignments are discussed in References 12-14, but are not of direct interest here, since the present study is concerned with fragment fluorescence. There is a strong similarity between fragment fluorescence yield and absorption spectra. The arrows in Figure 2 denote wavelengths where decay curves were recorded. All the CN^* decay curves discussed to this point were obtained with an interference filter (passing only CN B → X fluorescence) in front of the fluorescence detector.

It was found that all decay curves which utilized the interference filter could be fitted well by Eq. (1).

$$I(t) = C_0 + C_1[\exp -t/\tau] \tag{1}$$

A typical $CN^*(B^2\Sigma^+)$ decay curve is shown in Figure 3. At each wavelength a plot of τ^{-1} vs pressure yielded a straight line; i.e., Stern-Volmer quenching behavior was observed.[15] A linear least-squares fit of τ^{-1} vs pressure was done at each excitation wavelength, and the results are shown in Figure 4 and summarized in Table 1. In addition, a linear least-squares fit of τ^{-1} vs pressure was done using data points from all four excitation wavelengths. This fit is shown in Figure 5 and the results are given in Table 1. When the filter was not in place, two-component decays were observed, consisting of the $CN^*(B^2\Sigma^+)$ decay component and a very fast component with $\tau < 2$ nsec (see Fig. 6). The lifetimes of this short component were not accurately determined because our instrumental response function was too long (approximately gaussian

in time with ~4 nsec FWHM). However, the integrated intensities of the short components were obtained by fitting the long ($CN^*(B^2\Sigma^+)$) components, subtracting out their contributions (as well as the constant backgrounds), and summing the photon counts remaining (which are attributed to the fast decay). Then, the integrated intensity of the long component is obtained simply from Eq. (2)

$$I^{t_o t}_{CN(B^2\Sigma^+)} = \int_o^\infty c_1 e^{-t/\tau} dt = c_1\tau \qquad (2)$$

The results of these calculations are given in Table 2. The validity of these results are discussed in Section IV.

B. XeF_2

The XeF^* decay curves were fitted to an equation of the form

$$I(t) = C_0 + C_1 \exp(-t/\tau_1) + C_2 \exp(-t/\tau_2) \qquad (3)$$

A typical decay curve with its least-squares fit is shown in Figure 7. Plots of both τ_1^{-1} and τ_2^{-1} vs pressure yielded straight lines (see Fig. 8). Each set of data was fitted with linear least-squares and the results are $\tau_1 = 14.2 \pm 0.2$ nsec and $\tau_2 = 98 \pm 10$ nsec. These fits yield decay parameters with larger relative uncertainties than the $CN^*(B^2\Sigma^+)$ data which is attributed to the correlation between a large background parameter and the exponential decay parameters.

IV. Discussion

A. ICN

The kinetic analysis of the ICN data is quite straightforward. The photodissociation can be viewed as instantaneous;[16] thus, the 0.4 nsec

excitation pulse defines the time zero of $CN^*(B^2\Sigma^+)$ production. At this juncture, we note that the predissociation event is not being analyzed and will not be discussed at length, but the photodissociation event is significant in that it is much faster than the fluorescence process of $CN^*(B^2\Sigma^+)$. Quantitatively, we note that the convolution integral

$$I^{obs}(t) = \int_o^t \exp[-(t-t')/\tau_{B^2\Sigma^+}] \, f(t') \, dt' \tag{4}$$

given the intensity of $CN^*(B^2\Sigma^+)$ fluorescence as a function of time, where $f(t')$ is the convoluting function, the function describing the production of $CN^*(B^2\Sigma^+)$ as a function of time. If we equate $f(t') = \delta(t_o - t')$, then the trivial result is obtained that $I(t) \propto \exp[-t/\tau_{(B^2\Sigma^+)}]$.

The results of Section III-A can thus be rationalized using the following kinetic scheme

$$h\nu + ICN \xrightarrow{\text{instantaneous}} \begin{cases} I(^2P_{1/2,3/2}) + CN^*(B^2\Sigma^+) \\ I(^2P_{1/2,3/2}) + CN^*(A^2\Pi) \\ I(^2P_{1/2,3/2}) + CN\ (X^2\Sigma^+) \end{cases} \tag{5a}$$

$$CN^*(B^2\Sigma^+) \xrightarrow{\tau^{-1}(B^2\Sigma^+)} CN(X^2\Sigma^+) + h\nu \tag{5b}$$

$$ICN + CN^*(B^2\Sigma^+) \xrightarrow{k_q^{ICN}} CN(X^2\Sigma^+,\ A^2\Pi) + ICN \tag{5c}$$

which yields the fluorescence intensity given by

$$I(t) = I^0 \exp[-t/\tau(P)] \tag{6a}$$

where

$$[\tau(P)]^{-1} = \tau^{-1}_{(B^2\Sigma^+)} + k_q^{ICN} \cdot P. \tag{6b}$$

Production of $CN^*(B^2\Sigma^+)$ by collisional conversion of $CN^*(A^2\Pi)$ has been neglected in this analysis for reasons noted by Duric et al.[11] Thus, the intercepts derived in Section III-A (see Table 1) are estimates of $\tau^{-1}_{B^2\Sigma^+}$ and the slopes are quenching constants, k_q^{ICN}. The lifetime values vary with excitation wavelength. It is likely that this is caused by population of different rotational and vibrational distributions in the $CN^*(B^2\Sigma^+)$ manifold.

Radford and Broida have shown[17] that selected vib-rotational levels in the $CN^*(B^2\Sigma^+)$ are strongly mixed with vib-rotational levels of the $A^2\Pi$ system due to "L-uncoupling" terms in the molecular Hamiltonian. Jackson measured lifetimes of the individual rotational levels in the $CN^*(B^2\Sigma^+, v' = 0)$ manifold and found that the perturbed rotational levels have lifetimes longer than the unperturbed rotational levels. However, many rotational levels are populated by the photodissociation.[23] Since the measured lifetime is a weighted average over the manifold of populated rotational levels and the density of perturbed rotational levels is small, it is unlikely that the variations in our measured lifetimes are due to perturbations of isolated rotational levels.

A more likely explanation is that the vibrational distribution changes with the excitation wavelength. This results in a change in the lifetime because of variations of lifetime with vibrational level (see Ref. 11, for example). Therefore, the present results suggest that an investigation of vibrational distributions obtained with well-defined excitation wavelength be performed (as opposed to the work of Mele and Okabe,[23] where more than one discrete line was present in their resonance lamp excitation source).

Since our work cannot be unfolded to yield lifetimes of individual vibronic levels, we simply report the nominal lifetime of the $CN^*(B^2\Sigma^+)$ state as 70.5 ± 1.6 nsec (see last line of Table 1), and a quenching constant of 1.15×10^{-9} $cm^3 - s^{-1}$, which is in good agreement with the work of Jackson and Faris.[24] The lifetime that we report result is larger than most of the results listed in Table 3. A possible reason for this discrepancy is that our work did not utilize a monochromator to analyze the fluorescence wavelength. The CN^* fragments have a great deal of translational energy following photodissociation[23,24] and the same is presumably true of electron-impact dissociation. As shown by Mele and Okabe,[23] the CN fragment has approximately 1 eV in translational energy, and will move distances on the order of millimeters during its radiative lifetime. Depending on the position of the monochromator entrance slits and focusing optics leading to them, an excited CN^* fragment might be out of the field of view of the monochromator if it fluoresces many nanoseconds after excitation. *Thus, an apparent shortening of the lifetime will be observed due to the high degree of translational energy imparted to the $CN^*(B^2\Sigma^+)$ fragment.*

This reasoning draws support from other investigators. The work of Luk and Bersohn[16] utilized both ICN and BrCN as $CN^*(B^2\Sigma^+)$ sources. One expects that the CN^* fragment obtains more momentum (velocity) when it is fragmented from the heavier partner, i.e., the I atom. If the reasoning of the previous paragraph is correct, then the lifetime determined by Luk and Bersohn from the ICN sample should be shorter than that obtained from their BrCN sample. In fact, they observed that $\tau_{(B^2\Sigma^+)}$ = 59.9(21) nsec when ICN was used and $\tau_{(B^2\Sigma^+)}$ = 61.7(9) nsec when BrCN was the $CN^*(B^2\Sigma^+)$ source. Although the use of an interference filter in

the fluorescence channel might yield less detailed information about specific rovibronic lifetimes, it won't introduce the artifact of a short lifetime since the excitation region and the fluorescing region are both in the field of view of the detector. For completeness, it is noted that the work of Jackson[18] was performed with thermalized CN fragments, thus these arguments in no way invalidate his conclusions.

Some of our work did not utilize interference filters as discussed in Section III-A. A two-component decay was then observed. The additional component is attributed to fluorescence of ICN molecules that do not predissociate. Because our phototube could not detect the resonance fluorescence of ICN, but only fluorescence to high vibrational levels of the ICN ground electronic state manifold, the ratios listed in Table 2 are lower limits to the true branching ratio of fluorescence to predissociation. No efforts at calibrated actinometry were performed, but the present results provide impetus for further work.

B. XeF_2

Decay of $XeF^*(B^2\Sigma^+$ and $C^2\Pi_{3/2})$ can be modeled simply using the following scheme:

$$XeF_2 + h\nu \longrightarrow \begin{cases} XeF^*(B^2\Sigma^+) + F \\ XeF^*(C^2\Pi_{3/2}) + F \end{cases} \quad \text{(instantaneous)} \tag{7a}$$

$$XeF^*(B^2\Sigma^+) + XeF_2 \xrightarrow{k_3} XeF^*(C^2\Pi_{3/2}) \tag{7b}$$

$$XeF^*(C^2\Pi_{3/2}) + XeF_2 \xrightarrow{k_4} XeF^*(B^2\Sigma^+) \tag{7c}$$

$$XeF^*(B^2\Sigma^+) + XeF_2 \xrightarrow{k_5} XeF(X^2\Sigma^+) + XeF_2 \tag{7d}$$

$$XeF^*(C^2\Pi_{3/2}) + XeF_2 \xrightarrow{k_6} XeF(X^2\Sigma^+) + XeF_2 \tag{7e}$$

$$XeF^*(B^2\Sigma^+) \xrightarrow{k_7 (=\tau^{-1}_{B^2\Sigma^+})} XeF(X^2\Sigma^+) + h\nu' \tag{7f}$$

$$XeF^*(C^2\Pi_{3/2}) \xrightarrow{k_8 (=\tau^{-1}_{C^2\Pi_{3/2}})} XeF(A^2\Pi) + h\nu'', \tag{7g}$$

where Eqs. (7a) refer to excitation, (7b) and (7c) to collisional conversion, (7d) and (7e) to collisional quenching, (7f) and (7g) to radiative decay. As in the preceding subsection, the formation of the excited state radicals is assumed to be instantaneous. This kinetic model yields the following simultaneous differential equations:

$$\frac{-\partial C_B}{\partial t} = [k_7 + (k_3 + k_5)C_{XeF_2}]C_B - k_4\, C_{XeF_2}\, C_c \tag{8a}$$

$$\frac{-\partial C_C}{\partial t} = [k_8 + (k_4 + k_6)C_{XeF_2}]C_C - k_3\, C_{XeF_2}\, C_B \tag{8b}$$

where C_i denotes the concentration of the i^{th} species. (For brevity, B and C denote the $XeF^*(B^2\Sigma^+_{1/2})$ and $XeF^*(C^2\Pi_{3/2})$ respectively.) The solutions to these equations are[25]

$$C_i = k_i^+ e^{m_+ t} + k_i^- e^{m_- t} \tag{9}$$

where

$$i = XeF^*(B^2\Sigma^+),\ XeF^*(C^2\Pi_{3/2})$$

and

$$m_\pm = \frac{-(a+c) \pm [(a-c)^2 + 4bd]^{1/2}}{2} \tag{10}$$

where

$$a = k_7 + (k_3 + k_5)\ C_{XeF_2} \tag{11a}$$

$$b = k_4\ C_{XeF_2} \tag{11b}$$

$$c = k_8 + (k_4 + k_6)\ C_{XeF_2} \tag{11c}$$

$$d = k_3\ C_{XeF_2} \tag{11d}$$

which can easily be equated with coefficients of the concentration variables in Eqs. (8a) and (8b). One can see from Eq. (10) that $m_+ = -c$ and $m_- = -a$ when $4bd << (a-c)^2$. This condition is met, and can be verified by using our values of a and c (to be derived shortly) and using nominal values of transfer rates, b and d, from the literature. Thus, Eq. (9) can be written as

$$\begin{aligned} C_i = {} & k_i^+ \exp\{-[k_8 + (k_4 + k_6)\ C_{XeF_2}]t\} \\ & + k_i^- \exp\{-[k_7 + (k_3 + k_5)\ C_{XeF_2}]t\} \end{aligned} \tag{12}$$

The light intensity, I(t), can be written

$$I(t) = E_B \frac{\partial C_B}{\partial t} + E_C \frac{\partial C_C}{\partial t} \tag{13}$$

where the E_i's represent the efficiency of the photomultiplier tube detector to radiations from the B and C states. Since our phototube had an uncalibrated spectral response,

$$\begin{aligned} I(t) = {} & k_1 \exp\{-[k_8 + (k_4 + k_6)\ C_{XeF_2}]t\} \\ & + k_2 \exp\{-[k_7 + (k_3 + k_5)\ C_{XeF_2}]t\} \end{aligned} \tag{14}$$

where k_1 and k_2 do not provide any information since no detector calibration was performed. This in no way detracts from the information contained in the arguments of the exponentials as a function of pressure. We note that Eq. (14) implies that a two-exponential decay will be observed and that both decay components will vary linearly with pressure, as was observed. Thus, we conclude that τ_1 and τ_2 (see Section III-B) are equated with $\left[k_7 + (k_3+k_5)\ C_{XeF_2}\right]$ and $\left[k_8 + (k_4+k_6)\ C_{XeF_2}\right]$, respectively. Therefore $\tau_{B^2\Sigma^+} = 14.2(2)$ nsec and $\tau_{C^2\pi_{3/2}} = 98(10)$ nsec, which are in good agreement with previous investigations, as seen in Table 4. As was previously noted, the pressure was uncalibrated for the XeF_2 measurements, so the absolute values of the slopes of τ_i^{-1} vs pressure plots are unreliable. The radiative lifetimes obtained are reliable, since they are derived from the intercepts, not the slopes of the extrapolations.

V. Conclusions

The lifetime and ICN quenching constant of $CN^*(B^2\Sigma^+)$ have been determined to be 70.5(16) nsec and $1.15(4) \times 10^{-9}$ cm^3/sec, respectively. This lifetime is in fair agreement with earlier investigations although some discrepancy remains. It is possible that the high translational temperature of CN following dissociation led to artifacts in the previous investigations.

The lifetimes of the XeF^* $B^2\Sigma^+$ and $C^2\pi_{3/2}$ states have been measured as 14.2(2) nsec and 98(10) nsec, in good agreement with calculations of Dunning and Hay[2] and in good agreement with previous investigations.

This work illustrates that synchrotron radiation shows promise as a tool for generating and probing these excited state radicals. However,

the nonspecificity of the photodissociation event implies that many rovibronic levels of the fragment will be populated. If one wishes to do detailed studies (e.g., monochromatized fluorescence for state distributions), intensity considerations preclude the use of synchrotron radiation for many systems due to intensity considerations.

The timing characteristics of some synchrotron radiation facilities are superior to any existing VUV lasers and allow the study of electronic relaxation processes occurring on a nanosecond time scale.

Table 1. Results of Linear Least-Squares Fits of τ^{-1} vs P (Stern-Volmer plots, see Figures 4 and 5).

λ_{ex}(Å)	$\tau^{rad}_{CN(B^2\Sigma^+)}$(nsec)	k_q^{ICN}(cm^3-s^{-1})
1698	70.1(10)	$1.15(2) \times 10^{-9}$
1575	66.9(15)	$9.8\ (4) \times 10^{-10}$
1480	71.8(20)	$1.15(5) \times 10^{-9}$
1402	73.3(14)	$1.31(3) \times 10^{-9}$
*	70.5(16)	$1.15(4) \times 10^{-9}$

*Data from all four wavelengths used in a single fit of τ^{-1} vs P.

Table 2. Ratio of Integrated Intensities of CN Decay Components

λ_{ex}(Å)	$I^{tot}_{short}/I^{tot}_{CN(B^2\Sigma^+)} \times 10^2$
1698	28
1575	3
1480	7
1402	9

Table 3. Summary of $CN^*(B^2\Sigma^+)$ Lifetime Measurements

$\tau_{CN^*(B^2\Sigma^+)}$ (nsec)	Method	Remarks	Ref.
65.6(10)	Pulsed laser-induced fluorescence[a]	v' = 0	18
60.8(20)	Pulsed VUV photolysis (broadband) of ICN and BrCN[a]	Several vibrational states of CN probed	16
85(6)	Pulsed electron-bombardment[a]	Several vibrational states of CN probed	19
59.3(60)	Phase-shift technique with electron bombardment excitation	v' = 0,1,2	20
61.1(76)	Photon-photon delayed coincidence following electron bombardment excitation	v' = 0,1	21
63.8(6)	Pulsed electron bombardment excitation[a]	v' = 0	11
82(9)	Phase-shift using electron impact	v' = 0,1,2,3,4	22
70.5(20)	See text	Several vibrational states of CN probed	Present Work

[a]Fluorescence decay directly observed.

Table 4. Compilation of XeF Lifetime Results

$\tau_{XeF^*B^2\Sigma^+}$(nsec)	$\tau_{XeF^*C^2\pi_{e/2}}$(nsec)	Method	Remarks	Ref.
14.25(20)		XeF_2 photolysis at 1750 Å		26
19.4 (10)		Laser-induced fluorescence	a	27
16.5 (50)		Pulsed electron bombardment excitation of XeF_2		28
18.8		XeF_2 photolysis at 1930 Å	a	29
15.0 (8)				30
13.5(10)	100-150			31
12	113	Calculation (Hartree-Fock with CI, semi-empirical inclusion of spin-orbit effects)		2
14.2(2)	98(10)	See text		Present Work

[a]At time of these references, the $A^2\pi_{3/2,1/2}$ were denoted as two states and the $B^2\Sigma^+_{1/2}$ was denoted as the C state.

References for Chapter 4

1) a) J. A. Myer and R. W. Nicholls, Nature 225, 928 (1970) and references therein.

b) R. J. Spindler, J. Quant. Spectrosc. Radiat. Transfer 5, 165 (1965) and references contained therein.

2) T. H. Dunning and P. J. Hay, J. Chem. Phys. 69, 134 (1978).

3) C. H. Becker, P. Casavecchia, and Y. T. Lee, J. Chem. Phys. 69, 2377 (1978).

4) a) E. Matthias, R. A. Rosenberg, E. D. Poliakoff, M. G. White, S.-T. Lee, and D. A. Shirley, Chem. Phys. Lett. 52, 239 (1977).

b) E. Matthias, M. G. White, E. D. Poliakoff, R. A. Rosenberg, S.-T. Lee, and D. A. Shirley, Chem. Phys. Lett. 54, 30 (1978).

c) R. A. Rosenberg, M. G. White, E. D. Poliakoff, G. Thornton, and D. A. Shirley, J. Phys. B11, L719 (1978).

5) "Fluorescence Decay of the 0_u^+ and 1_u States of Xe_2" G. Thornton, E. D. Poliakoff, E. Matthias, S. H. Southworth, R. A. Rosenberg, M. G. White, and D. A. Shirley, J. Chem. Phys., 71, 133 (1979).

6) H. D. Wenck, S. S. Hasnain, M. M. Nitikin, K. Sommer, G. Zimmerer, and D. Haaks, DESY Report SR-79/07 (1979).

7) T. D. Bonfield, F. H. K. Rambow, G. K. Walters, M. V. McCusker, D. C. Lorents, and R. A. Gutchek, SSRL Report 78/09 (1978).

8) K. M. Monahan and V. Rehn, J. Chem. Phys. 68, 3814 (1978).

9) The time structure of a synchrotron is dependent on the length of the orbit as well as the number of electron bunches circulating through the accelerating ring. Several facilities have physical parameters well-suited for studying events on a nanosecond time scale. A review of synchrotron radiation properties is given in: I. Lindau and H. Winick, Comments Atomic Mol. Phys. 6, 133 (1977).

10) G. A. West and M. J. Berry, Chem. Phys. Lett. 56, 423 (1978).

11) N. Duric, P. Erman, and M. Larsson, Physica Scripta 18, 39 (1978).

12) G. W. King and A. W. Richardson, J. Mol. Spec. 21, 339 (1966).

13) M. T. Macpherson and J. P. Simons, J. Chem. Soc., Faraday II, in press.

14) J. W. Rabalais, J. M. McDonald, V. Scherr, and S. P. McGlynn, Chemical Reviews 71, 73 (1971).

15) J. G. Calvert and J. Pitts, Photochemistry (John Wiley and Sons, Inc., New York, 1966).

16) C. K. Luk and R. Bersohn, J. Chem. Phys. 58, 2153 (1973). The authors analyze the build-up time of the fluorescence to determine $\tau_{ICN} \leq 5 \times 10^{-10}$ sec.

17) H. E. Radford and H. P. Broida, Phys. Rev. 128, 231 (1962).

18) W. M. Jackson, J. Chem. Phys. 61, 4177 (1974).

19) R. G. Bennett and F. W. Dalby, J. Chem. Phys. 36, 399 (1962).

20) H. S. Liszt and J. E. Hesser, Astrophys. J. 159, 1101 (1970).

21) K. A. Mohamed, G. C. King, and F. H. Read, J. Elec. Spec. & Rel. Phen. 12, 229 (1977).

22) J. H. Moore and D. W. Robinson, J. Chem. Phys. 48, 4870 (1968).

23) A. Mele and H. Okabe, J. Chem. Phys. 51, 4798 (1969).

24) W. M. Jackson and J. L. Faris, J. Chem. Phys. 56, 95 (1972).

25) A similar kinetic analysis can be found in: M. Stock, E. W. Smith, R. E. Drullinger, and M. M. Hessel, J. Chem. Phys. 68, 4167 (1978).

26) J. G. Eden and R. W. Waynant, Opt. Lett. 2, 13 (1978).

27) C. H. Fisher and R. E. Center, J. Chem. Phys. 69, 2011 (1978).

28) J. G. Eden and S. K. Searles, Appl. Phys. Lett. 30, 287 (1977).

29) R. Burnham and N. W. Harris, J. Chem. Phys. 66, 2742 (1977).

30) R. Burnham and S. K. Searles, Paper AA-3, 30th Annual Gaseous Electronics Conference, Palo Alto, CA (1977).

31) J. J. Ewing, 7th Winter Colloquium on Quantum Electronics, Park City, Utah (1977).

Figure Captions

Figure 1. Experimental schematic.

Figure 2. ICN excitation spectrum (fluorescence intensity vs excitation wavelength; uncorrected for variations in incident radiation flux).

Figure 3. ICN decay curve ($CN^*(B^2\Sigma^+)$ decay only).

Figure 4. Individual ICN Stern-Volmer fits.

Figure 5. Stern-Volmer fit (all four wavelengths).

Figure 6. Unfiltered decay curve with ICN as sample gas.

Figure 7. XeF^* decay curve.

Figure 8. XeF^* Stern-Volmer fits.

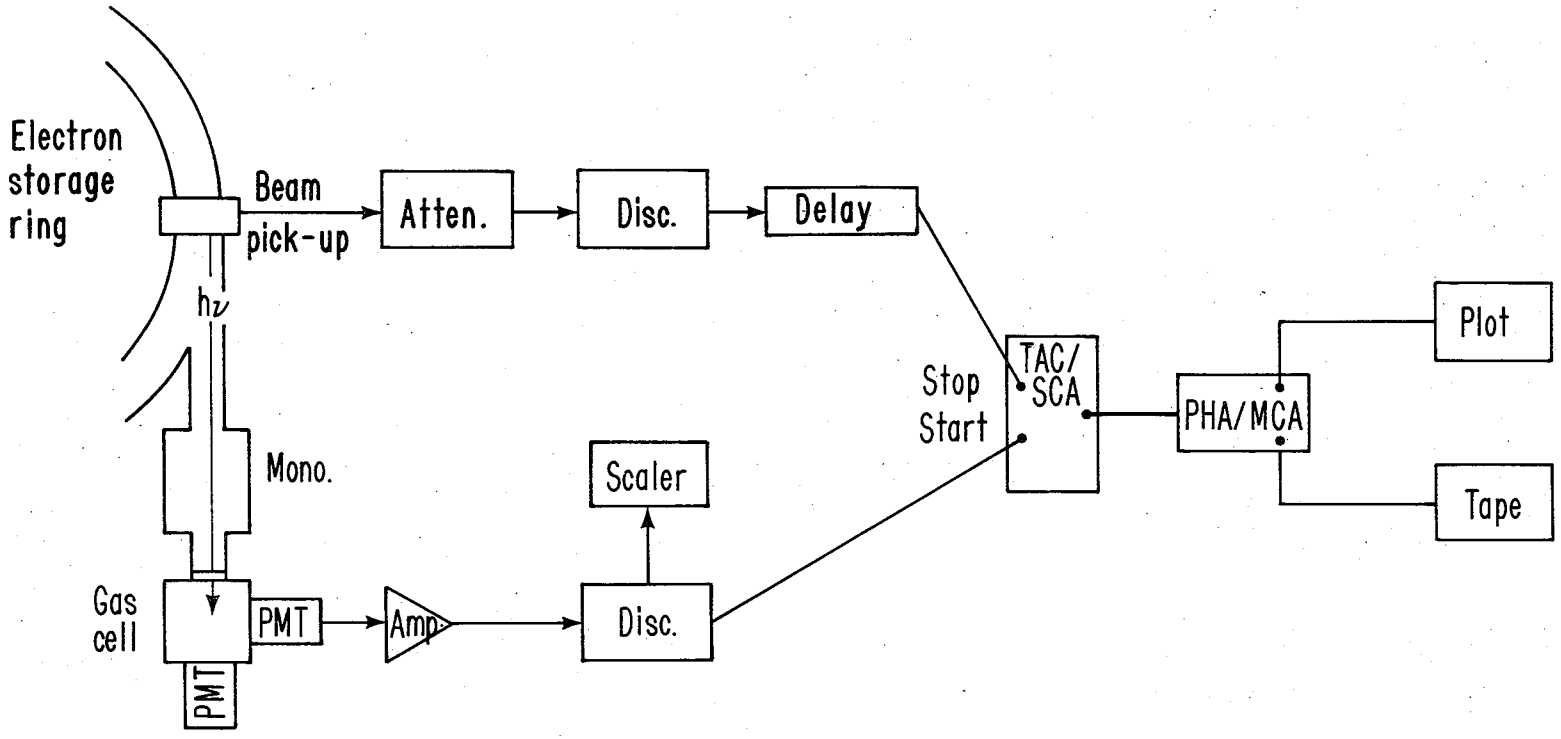
Electron
storage
ring
Beam
pick-up
Atten.
Disc.
Delay
hν
Mono.
Scaler
Gas
cell
PMT
Amp.
Disc.
PMT
Stop
Start
TAC/
SCA
PHA/MCA
Plot
Tape
XBL-7612-4530

Figure 1

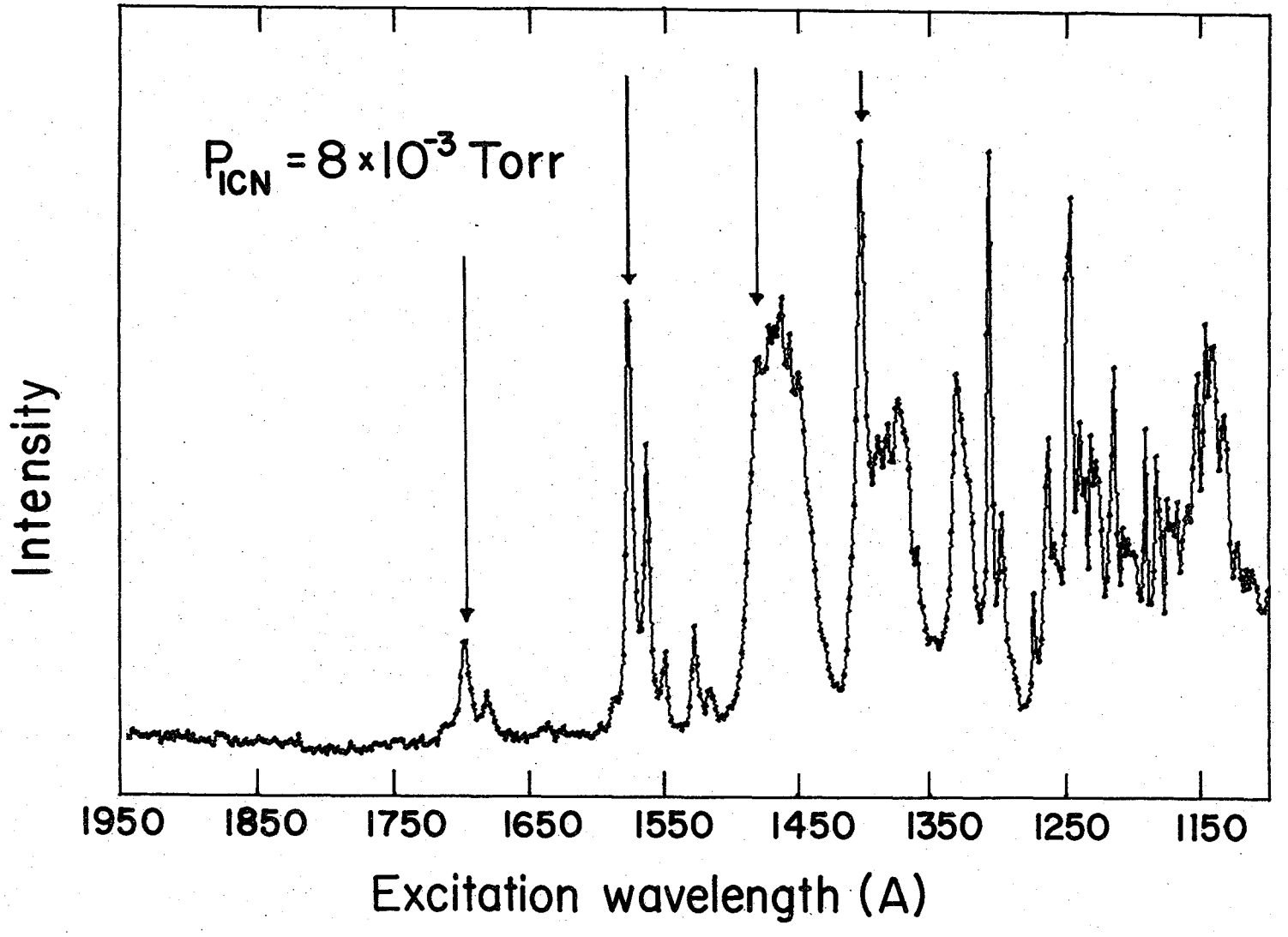

Figure 2

XBL 7810-11909

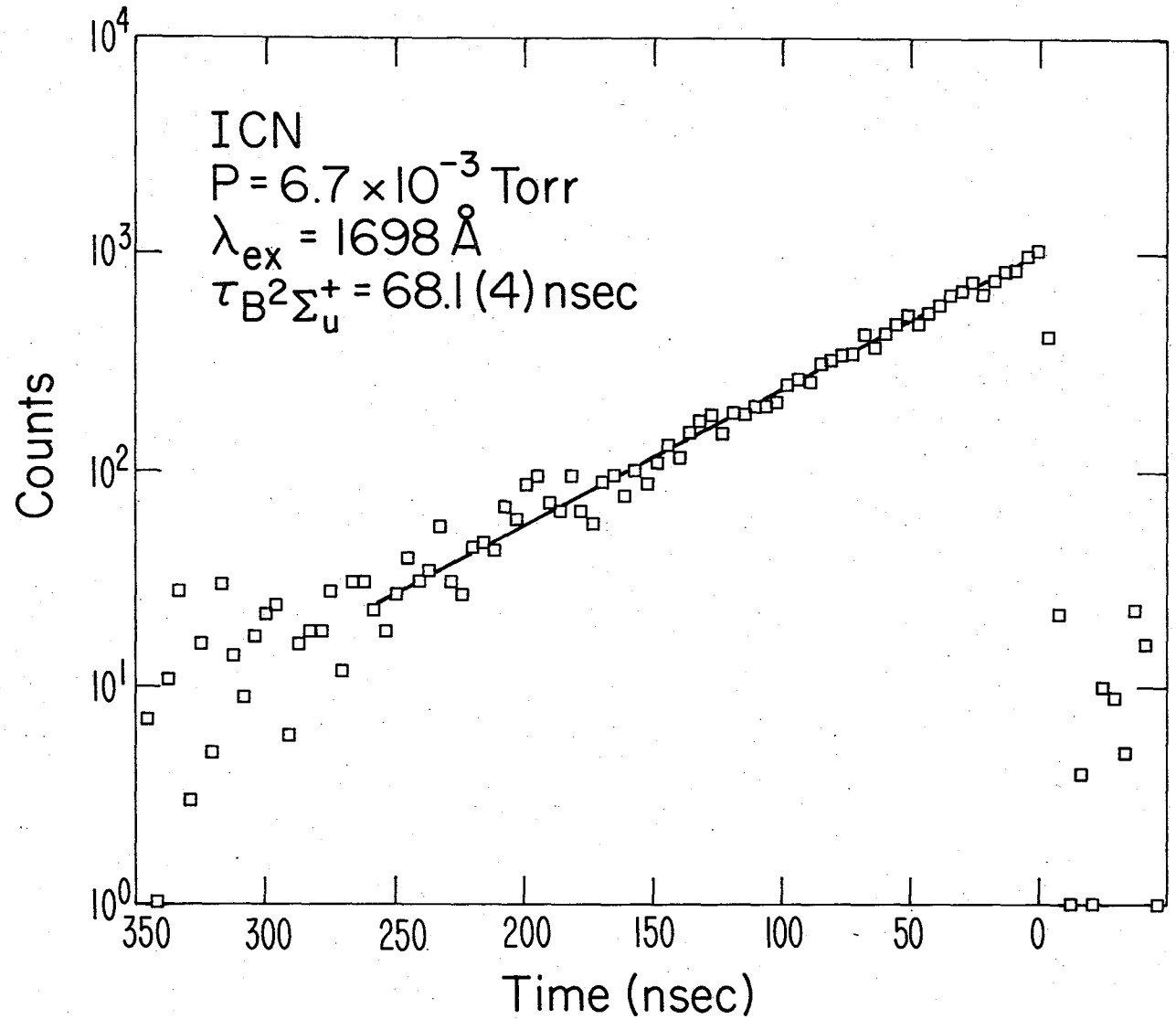

Figure 3

XBL797-2094

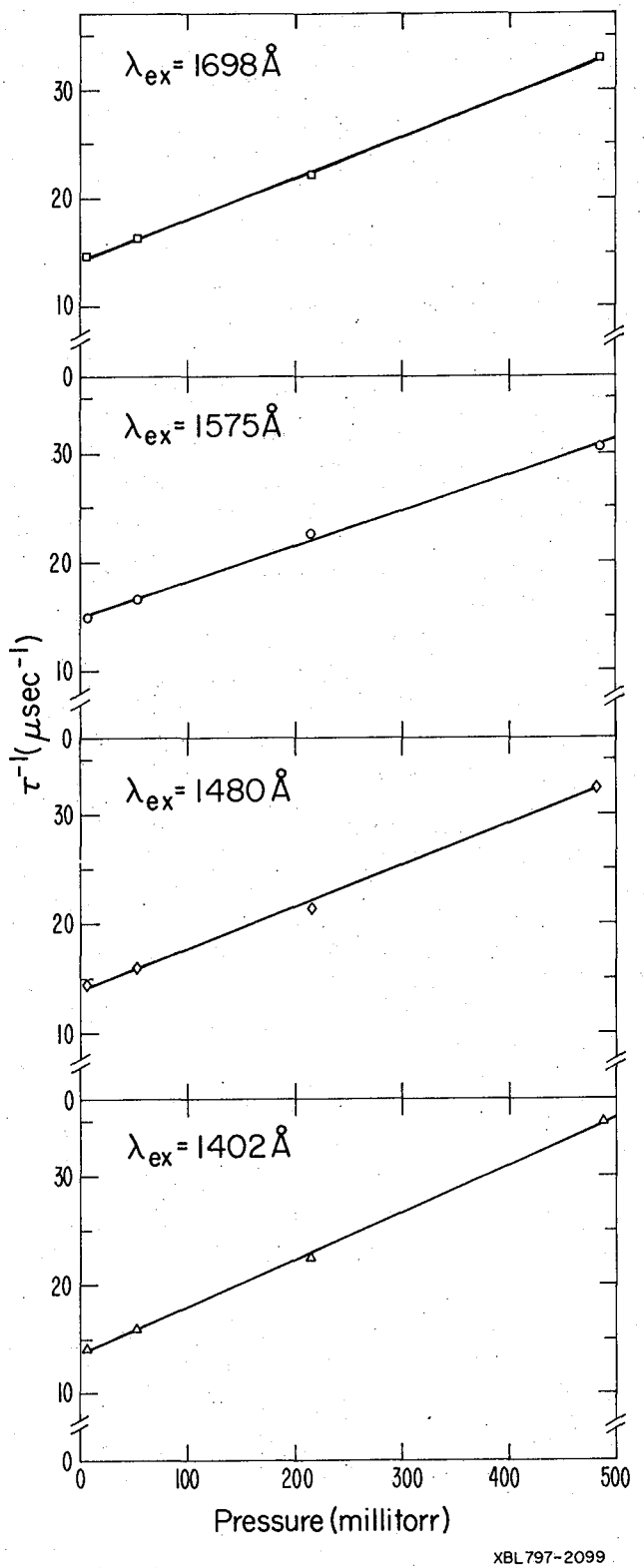
λex= 1698Å
λex= 1575Å
λex= 1480Å
λex= 1402Å
τ⁻¹(μsec⁻¹)
0
10
20
30
100
200
300
400
500
Pressure (millitorr)
XBL797-2099

Figure 4

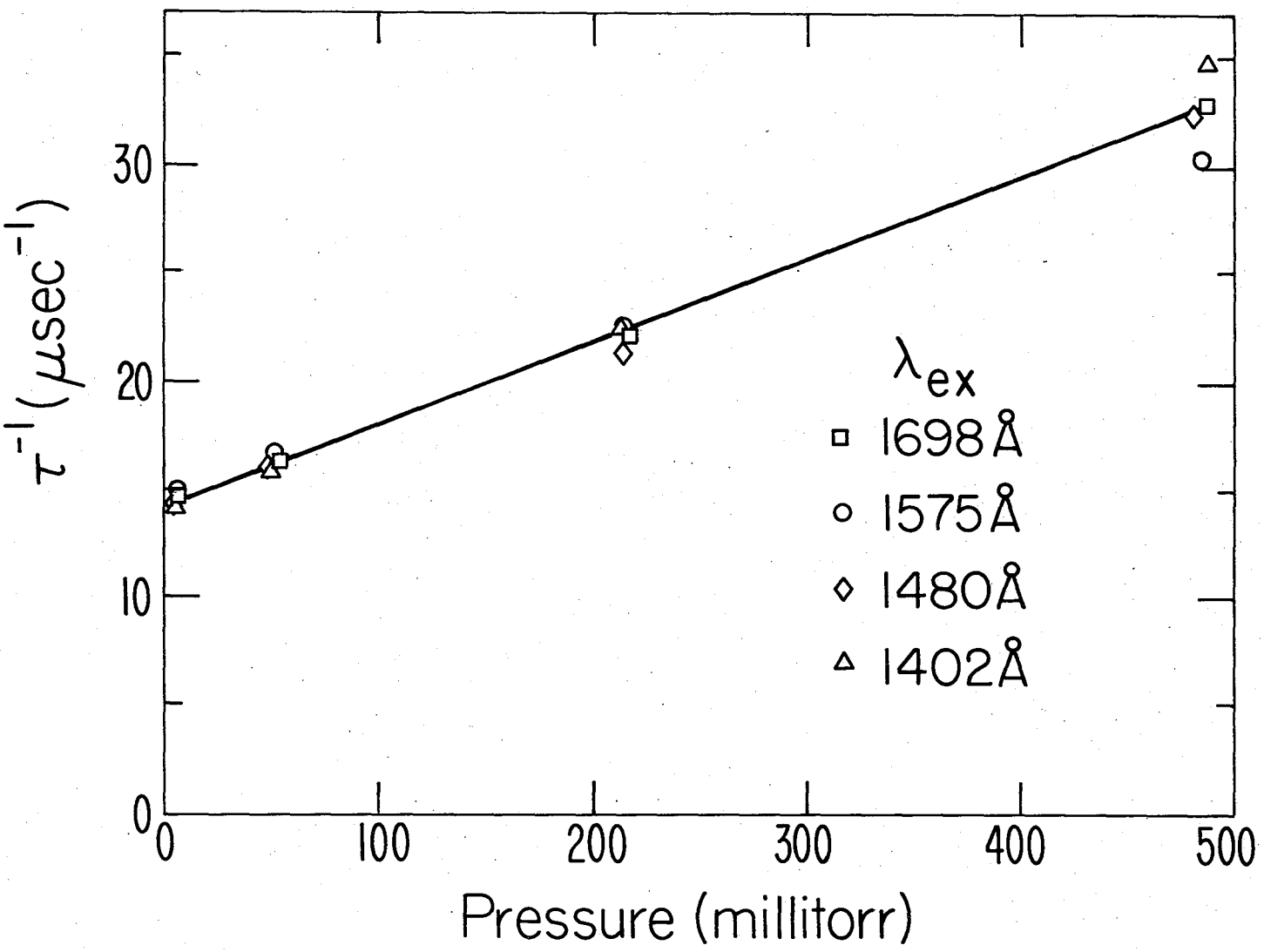

Figure 5 XBL797-2098

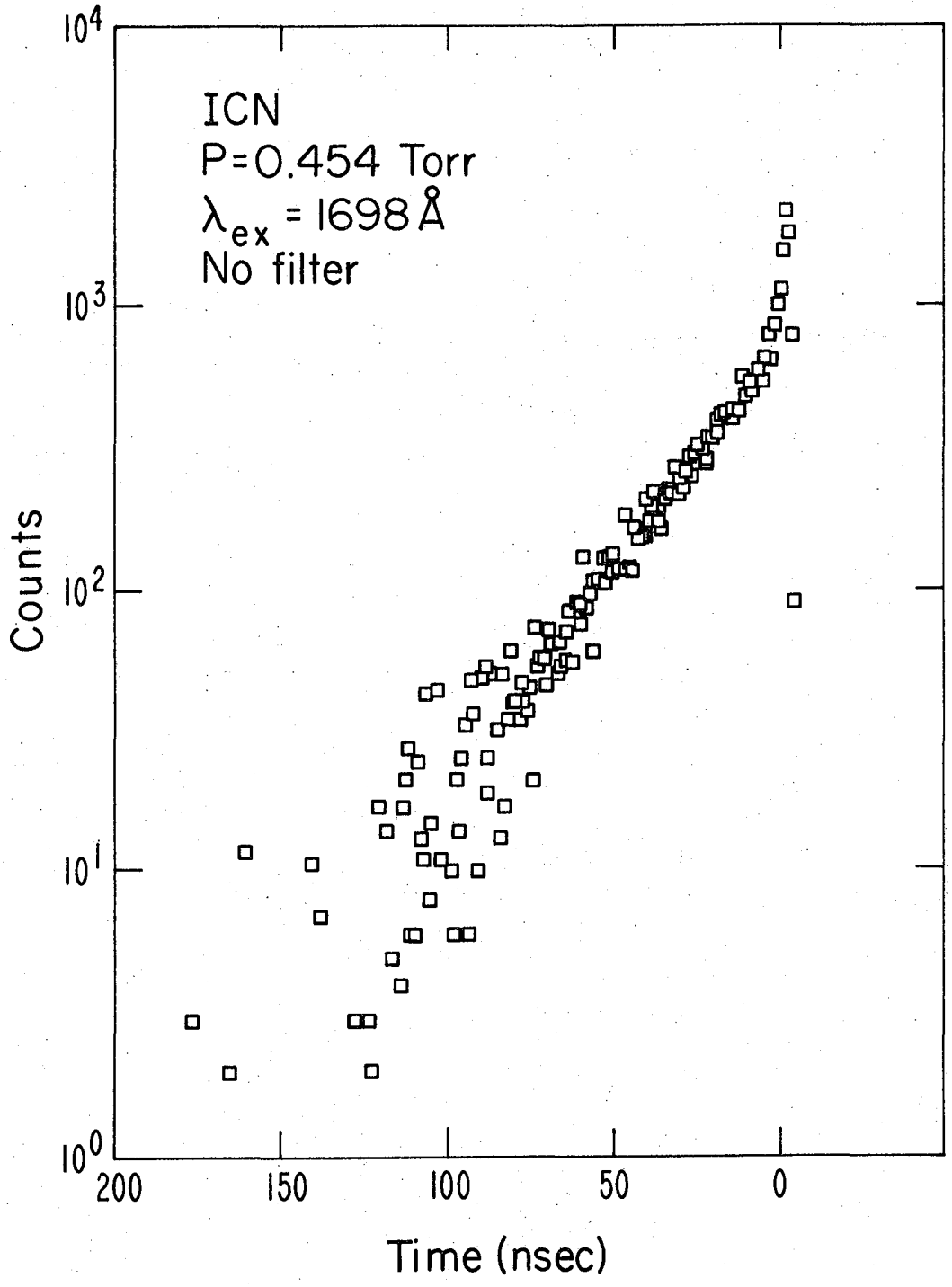

Figure 6 XBL797-2095

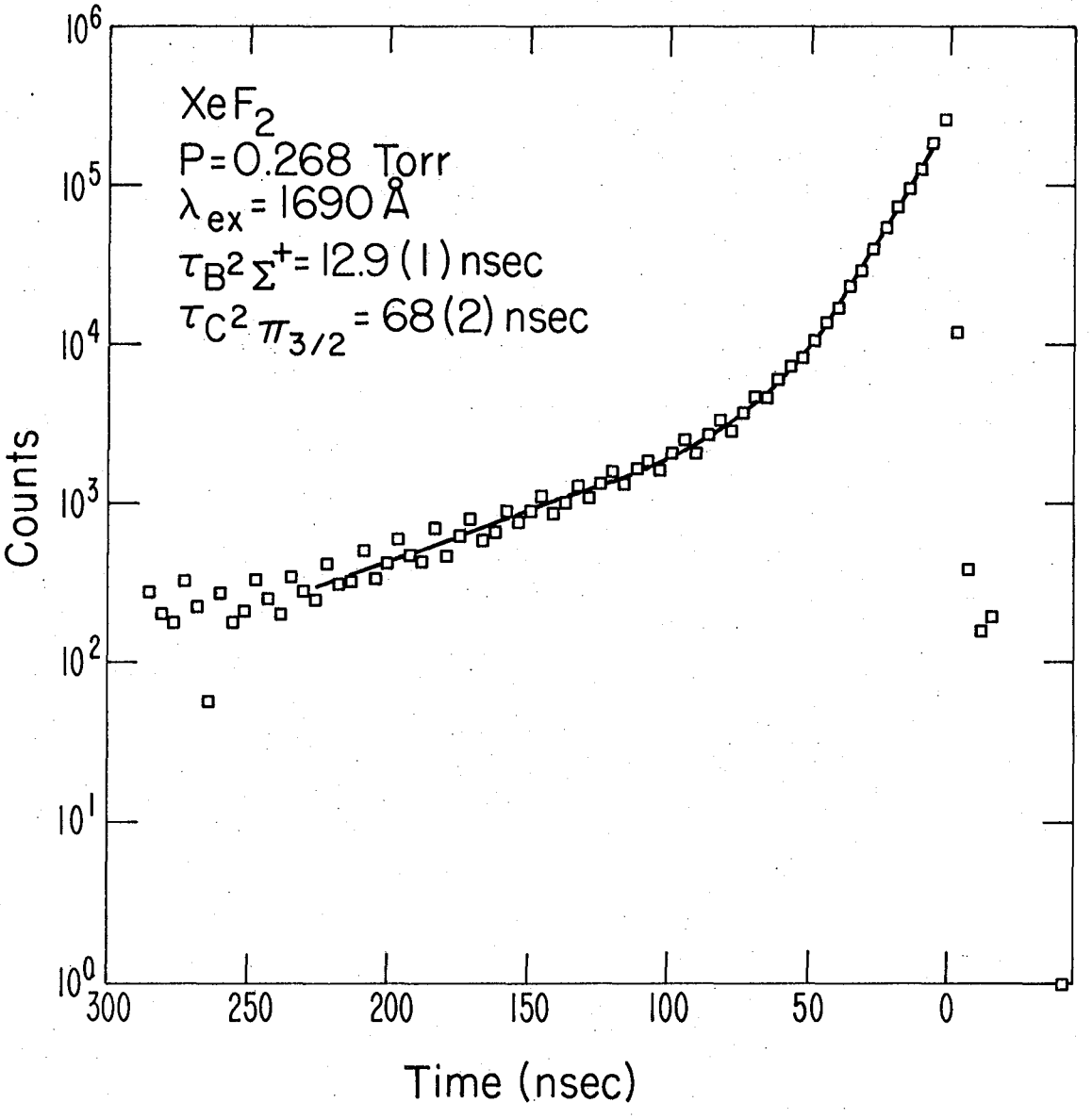

Figure 7 XBL 797-2096

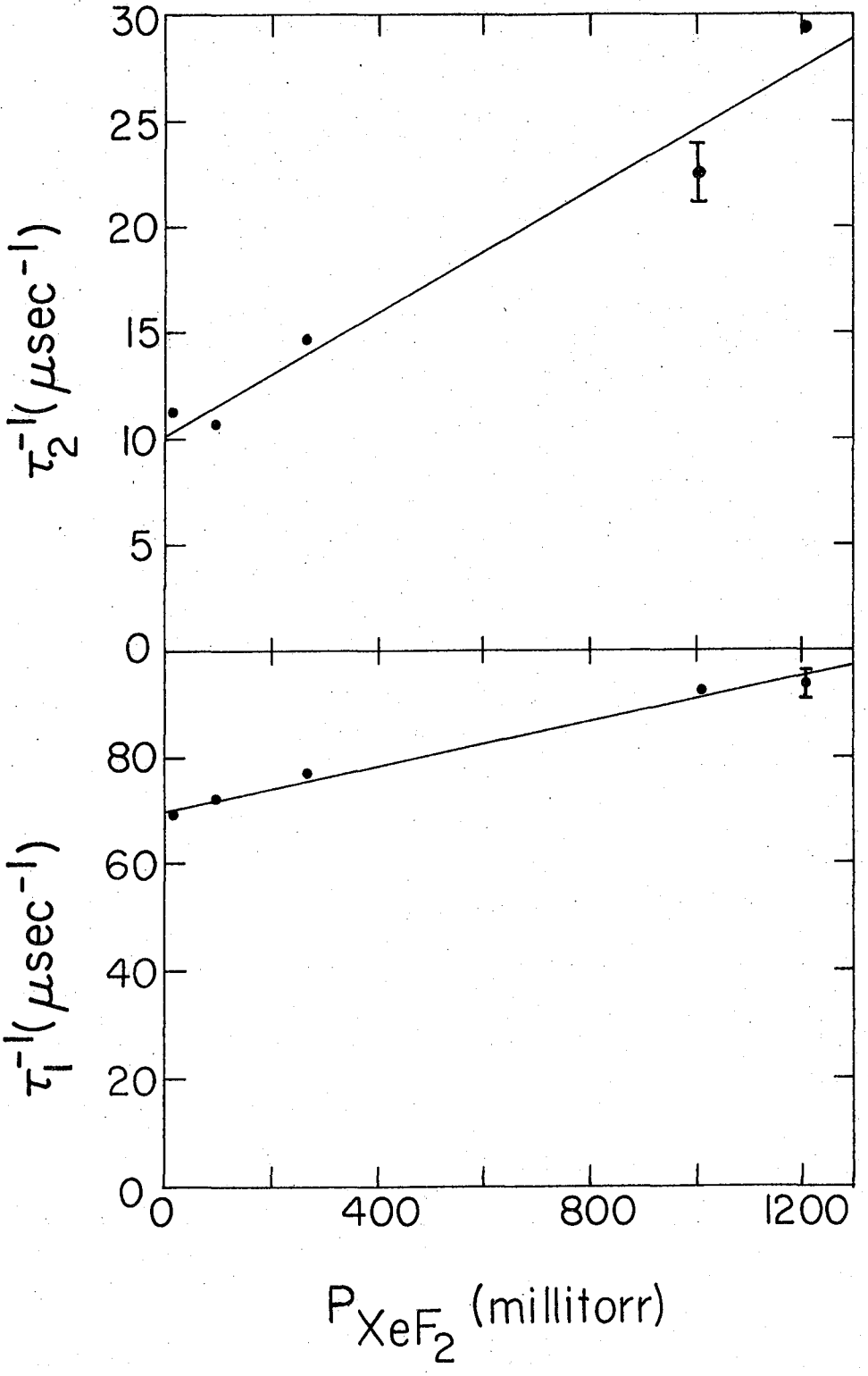

XBL 797-10657

Figure 8

Chapter 5

Polarized Fluorescence from Photodissociation Fragments: A Study of ICN Photolysis

I. Introduction

The last chapter illustrated that synchrotron radiation can be used to study fragments produced in the photodissociation process. In this chapter, it is shown that the fragment fluorescence is a probe of the photodissociation event itself. Specifically, the correlation between the excitation and fluorescence polarizations may elucidate the dynamics of simple photodissociative systems. It appears that the fluorescence polarization is related to the symmetry and lifetime of the photoexcited parent molecule, two parameters essential for an understanding of a photodissociative process.[1]

The basis for such experiments was first discussed by Van Brunt and Zare.[2] The experiment is related to photolysis mapping experiments of Solomon[3] and photofragmentation spectroscopy experiments of Wilson[4a] and Bersohn.[4b] All of these experiments depend on an anisotropic interaction of the radiation field with the target molecule (i.e., there are preferred directions of the molecule leading to photodissociation) coupled with an anisotropic distribution of the fragments. Since the experiment discussed in this chapter deals with the triatomic reaction $ICN + h\nu \rightarrow I + CN^*(B^2\Sigma^+)$, the remainder of this chapter considers an idealized triatomic system:

$$ABC(\Lambda_1) + h\nu_1(\underset{\sim}{\varepsilon}_1) \longrightarrow ABC^*(\Lambda_2) \qquad (1)$$

$$ABC^*(\Lambda_2) \xrightarrow{k_1} A + BC^*(\Lambda_3) \qquad (2)$$

$$BC^*(\Lambda_3) \xrightarrow{k_2} BC(\Lambda_4) + h\nu_2(\underset{\sim}{\varepsilon}_2), \qquad (3)$$

where Λ_i denotes the projection of the orbital angular momentum (or symmetry species, for triatomics of C_σ or C_{2v} symmetry), and $\underset{\sim}{\varepsilon}_i$ the polarization. The radiative lifetime of BC^* is k_2^{-1}, and the dissociative lifetime of $ABC^*(\Lambda_2)$, k_1^{-1}, is assumed to equal zero unless otherwise noted (i.e., the dissociation event is assumed to occur instantaneously). In most experiments, Λ_1, Λ_3, Λ_4, and $\underset{\sim}{\varepsilon}_1$ are known. $\underset{\sim}{\varepsilon}_2$ is determined through the fluorescence polarization measurement; thus, the only unknown in the process is Λ_2, the symmetry of the photoexcited surface.

Synchrotron radiation is ideally suited for the polarization experiments for several reasons.

1) The degree of linear polarization is usually quite high. In the case of the 8° branch line at SSRL, the polarization, P_{ex}, is greater than 0.95.
2) The pulse structure allows for decay curves to be taken and the polarization can be analyzed during the decay process. Thus, dark counts not occurring during the decay process are not collected and do not degrade the accuracy with which P_{fl} is determined.
3) The radiation is tunable.

The last point is significant if one wishes to sort out the effects of competing dissociation channels. Assuming a single dissociative channel exists in a certain energy range, the polarization measurement of the fluorescence at one excitation wavelength would suffice to characterize the symmetry of the dissociative surface. However, real systems frequently have many competing channels operating simultaneously, and

require measurements at a number of excitation wavelengths to deconvolute Franck-Condon effects that might emphasize a state of one symmetry (or equivalently, polarization) at one wavelength, the opposite polarization at another wavelength, and little or no polarization at intermediate wavelengths. Thus, the tunability of synchrotron radiation as well as its high degree of linear polarization afford an excellent opportunity for discerning the various channels and states involved.

The lack of excitation wavelength tunability is a drawback of the related technique, photofragment spectroscopy. In a photofragment spectroscopy measurement, one determines the symmetry, Λ_2, and lifetime, k_1^{-1}, by pulsed laser excitation of a molecular beam containing the parent molecule. The fragment intensity is monitored (by a mass spectrometer) as a function of the fragment flight time and the angle between $\underset{\sim}{\varepsilon}_1$ and the velocity vector of the fragment. Because the molecular beam density is frequently low and small collection angles must be used (for a meaningful angular dependence), the use of laser excitation is essential for obtaining photon fluxes adequate for good signal-to-noise-ratios. Tunable lasers in the UV and VUV wavelength regions with suitable photon fluxes are not available at the present time. Thus, the polarization technique reported in this chapter can extend our capabilities for studying the photodissociation process.

In addition, there are differences in the kinds of information gained from photofragment spectroscopy and polarization experiments. As opposed to photofragment spectroscopy, measurement of the fluorescence polarization yields information regarding the orientation of the diatomic rotational angular momentum[5] (the M_J value, in a quantum-mechanical sense). Perhaps some of the puzzling questions regarding

the high rotational excitation of molecular photolysis products,[6,7] as well as the possible explanations of this rotational excitation,[8] can be addressed with simple polarization studies.

There is a technical advantage to the polarization analysis technique, as well. The apparatus is not dependent on a collimated molecular beam (as is the case in photofragment spectroscopy). This simplifies the experiment considerably, a real "plus" for an experiment performed at a synchrotron radiation source.[9]

II. Classical Description of the Process

The fluorescence polarization, P_{fl}, is defined as

$$P_{fl} \equiv \frac{I_{\parallel} - I_{\perp}}{I_{\parallel} + I_{\perp}} , \tag{4}$$

where $I_{\parallel}$ and $I_{\perp}$ represent the intensities of fluorescence with $\underset{\sim}{\varepsilon}_2$ parallel and perpendicular to $\underset{\sim}{\varepsilon}_1$, respectively. If it is assumed that a classical description is valid,[10] the fluorescence polarization is related to the fragmentation process by Eq. (5).[5]

$$P_{fl} = \frac{3\langle\cos^2\gamma\rangle - 1}{\langle\cos^2\gamma\rangle + 3} . \tag{5}$$

Here, γ is the angle between $\underset{\sim}{\mu}_{abs}$ and $\underset{\sim}{\mu}_{fl}$ (the absorption and fluorescence dipoles, respectively), and $\langle\rangle$ denotes an ensemble average. Equation (5) is derived in the appendix to this chapter.

To clarify the argument, the absorption and transition dipole moments are "tied" to the molecular frame, which is rotating in the space-fixed coordinate system. For example, consider the ICN case. The $CN^*(B \rightarrow X)$ transition is a $\Sigma \rightarrow \Sigma$ transition, or parallel transition,

indicating that the transition dipole moment lies along the internuclear axis. The ground electronic state of ICN is linear, and let us suppose that the excited dissociative state is bent and that $\underset{\sim}{\mu}_{abs}$ lies in the plane of the bending motion. Then the $CN^*(B^2\Sigma^+)$ fragments will rotate in the plane of the bending motion, implying that $\underset{\sim}{\mu}_{abs}$ and $\underset{\sim}{\mu}_{cm}$ lie in the same plane.‡ Because the radiative lifetime of $CN^*(B^2\Sigma^+)$ is so much longer than the rotational period of the CN^* fragment, there is no correlation between $\underset{\sim}{\mu}_{abs}$ and $\underset{\sim}{\mu}_{fl}$ in the plane ("like the minute and hour hands of a clock[11]") so the average angle, γ, is $\Pi/4$, or $P_{fl} = 1/7$. The various possible cases applicable to direct dissociation have been catalogued[11] and are not reproduced here.

III. Experimental

Because of the excellent timing parameters, polarized fluorescence was measured as a function of time following the pulse, i.e., decay curves were generated for both the parallel and perpendicular fluorescence components. Thus, collisional and time-dependent depolarization could be investigated.[12]

The experimental apparatus was similar to that of Chapter 4. The traditional right-angle geometry was employed for excitation/observation (see Fig. 1). An interference filter (Microcoatings, Inc., #3850 BBC) was placed in front of the polarization analyzer (Melles Griot sheet polarizer, #03FPG003) and phototube (RCA #8850) to reject all radiation except $CN(B \rightarrow X)$ fluorescence. The interference filter (200 Å FWHM) has

---

‡ It is implicitly assumed that the photodissociation is impulsive, and that the rotational angular momentum of the parent molecule is much smaller than that of the product diatomic molecule.

its peak transmission at 3850 Å to transmit principally the $\Delta v = 0$ sequence.[13] Low fluorescence intensity necessitated the use of a large band-pass (8.7 Å FWHM) on the monochromator used to select the excitation wavelength. Extensive checks were made for spurious polarization signals. In particular, the stray light level was found to be negligible.

Data were collected at ICN pressures from 10 to 100 millitorr, measured using a capacitance manometer (MKS 315 BHS-10) and held constant by a servo-driven leak valve to pressure deviations of 0.5% or less.

IV. Results

The data analysis revealed no effects of pressure on the polarization; only the 50 millitorr results are presented here. The data were analyzed by subtracting the dark count background from both the parallel and perpendicular decay curves, then summing counts between t_1 = 6 nsec and t_2 = 50 nsec (see Fig. 2). It was found that other choices for t_1 and t_2 yielded the same value for the fluorescence polarization, but with poorer signal-to-noise ratios. We chose t_1 to be 6 nsec rather than 0 nsec to exclude Rayleigh-scattered stray light. The observed time-independent behavior suggests that the collisional quenching cross-section is so large[14,15] that the collisional depolarization (alignment destruction) is not competitive. The 50 millitorr results are shown graphically in Figure 3 and are summarized in Table 1. Corrections resulting from our finite acceptance angle ($\Theta = 11°$ half-angle) were found to be insignificant[16] ($\leq 1\%$) in comparison to the variations in reproducibility of the results, which are given as error bars in Figure 3.

V. Discussion

Several interesting trends can be noted in the results. First, the degree of vibrational excitation of the *parent* ICN, which subsequently predissociates, appears to have a profound effect on the degree of polarization observed in the neighborhood of 1400 Å. Second, populating the first three members of the lowest-lying Rydberg series (λ_{ex} = 1698 Å, 1331 Å, 1247 Å) all led to vanishing values of polarization in the diatomic fragment fluorescence. Finally, we note that the observed polarizations were all positive. Our results imply[17] that the transition dipole moment, μ_{abs}, lies in the triatomic plane or along the triatomic axis if the equilibrium geometry of the ICN dissociative state is bent or linear, respectively.

One sees from Figure 3 that all polarization measurements were done at wavelengths corresponding to peaks in the fluorescence excitation spectrum. This was done because the signal was low and the background (dark current from the phototube) was of comparable intensity. While simplifying the experiment, these choices of excitation wavelengths complicated the analysis of the data. This is because the states of $ICN^*(A_2)$ that are populated are not simply (directly) dissociative but predissociative. Using the reasoning of Section II, *one concludes that the measurement is sensitive not only to the symmetry of the dissociative surface but also to the symmetry and lifetime the predissociating state;* i.e., absorption takes $ICN^*(A_1)$ to a bound state $ICN^*(A_2)$ which, after rotating for the length of its dissociative lifetime, undergoes a non-radiative transition to $ICN^*(A_2')$, which is the dissociative electronic state. This rotation of the parent molecule prior to

dissociation will reduce the anisotropy of the fragment and the polarization.

So, the comparison of the reported results with Table 1 of Ref. 11b is not strictly valid. More recent measurements in the region of 1650 Å (no predissociating resonances are present; see Fig. 3) have yielded positive polarizations with values of $P \approx 0.09$. Thus, the claim that $\underset{\sim}{\mu}_{abs}$ involves a parallel transition appears to be correct.

VI. Conclusions

These results are preliminary, but are extremely encouraging, nonetheless. It appears that the polarization of fragment fluorescence is indeed a sensitive probe of the photodissociation event. Qualitative insight has been gleaned from simple classical modeling, but a full quantum treatment would be much more satisfying. In particular, a treatment of the predissociation process and its relation to $\langle\cos^2\gamma\rangle$ and P_{fl} would be most desirable.

APPENDIX

Derivation of Equation (5)[5]

In Section II, it was stated that

$$P_{f1} = \frac{3\langle\cos^2\gamma\rangle - 1}{\langle\cos^2\gamma\rangle + 3} . \tag{A1}$$

To prove this, we must first clarify the nature of the coordinate systems employed in the derivation. The space-fixed coordinate system has cartesian axes X, Y, and Z; the macroscopic observables are usually referenced to this coordinate system (e.g., polarization of excitation and fluorescence radiation, propagation vector of the radiation). The microscopic variables are attached to the molecule-fixed cartesian axes, x, y, and z (e.g., z is frequently chosen as the internuclear axis of linear molecules.) Probability of electronic excitation (or fluorescence) involves polarization of the radiation (in the space-fixed frame) as well as the electronic transition dipole (in the molecule-fixed frame). Thus, a prescription is necessary for the transformation between the molecule-fixed and space-fixed coordinate systems.

Since all of the quantitites that will be discussed are vector quantities, the discussion will be limited. One can describe a vector, $\underline{\mu}$, by the magnitude of its three cartesian components μ_x, μ_y, and μ_z, or its magnitude ($|\underline{\mu}|$) and three direction cosines, $\mu_x/|\underline{\mu}|$, $\mu_y/|\underline{\mu}|$, and $\mu_z/|\underline{\mu}|$. Since we are concerned with relative and not absolute fluorescence intensities, $I_{\parallel}$ and $I_{\perp}$, the latter description is appropriate. For brevity, we define $\lambda_g = \mu_g/|\underline{\mu}|$, where g = x, y, z. Thus, a vector $\underline{\mu}$ can be expressed as

$$\underset{\sim}{\mu} = |\underset{\sim}{\mu}| \sum_{g} \lambda_g \hat{g}, \tag{A2}$$

where g is an index running from x to z, and $\hat{g}$ represents a unit vector in the g direction.

Using the Euler angles,[18] (α, β, γ), we can view the vector, $\underset{\sim}{\mu}_{abs}$, in the space-fixed coordinate system using Equation (A3) and Table 1 of Ref. 19.

$$\underset{\sim}{\mu}_{abs} = |\underset{\sim}{\mu}_{abs}| \sum_{F} \sum_{g} \Phi_{Fg} \lambda_g^{abs} \hat{F}, \tag{A3}$$

where the Φ_{Fg} are direction cosine matrix elements.[19] For simplicity, the molecule fixed coordinate system is usually chosen so that $\underset{\sim}{\mu}_{abs} = \lambda_z^{abs} \hat{z}$. (There is no loss in generality in doing this, since the parent molecule angular orientation comprises an isotropic distribution and all orientations are averaged over.) Equation (A3) then simplifies to

$$\underset{\sim}{\mu}_{abs} = |\underset{\sim}{\mu}_{abs}| \sum_{F} \Phi_{Fz} \lambda_z^{abs} \hat{F}. \tag{A4}$$

If the excitation radiation is polarized along the space fixed Z axis, the probability for absorption of radiation is proportional to Φ_{Zz}^2. Let the fluorescence transition dipole lie in the direction $\underset{\sim}{g}$. Then the probability for the molecule fluorescing with the $\underset{\sim}{\varepsilon}$-vector parallel to Z is proportional to Φ_{Zq}^2. Consequently, the probability for emission of radiation with $\underset{\sim}{\varepsilon}$ vector parallel to $\underset{\sim}{\varepsilon}_1$ is given by

$$I_{\parallel} \propto \langle \Phi_{Zz}^2 \Phi_{Zq}^2 \rangle, \tag{A5}$$

and similarly, the probability for emission of radiation with $\underset{\sim}{\varepsilon}$-vector

perpendicular to $\underset{\sim}{\varepsilon}_1$ is

$$I_\perp \propto \langle \Phi_{Zz}^2 \, \Phi_{Xq}^2 \rangle. \tag{A6}$$

Here, the averages denoted by <> refer to all initial orientations of the parent molecule; i.e., one averages over $d\alpha \sin\beta d\beta d\gamma/8\pi^2$, where γ is the Euler angle and not the variable in Eqs. (A1).

To cast Eqs. (A5) and (A6) into a more useful form, we note that

$$\Phi_{Fq} = \sum_g \Phi_{Fg} \, \Phi_{gq}, \tag{A7}$$

where F represents Z or X and g = x, y, and z. Squaring, we obtain

$$\Phi_{Fq}^2 = \sum_{g_1} \sum_{g_2} \Phi_{Fg_1} \, \Phi_{Fg_2} \, \Phi_{g_1 q} \, \Phi_{g_2 q}, \tag{A8}$$

where g_1 = x, y, and z, g_2 = x, y, and z, but they are independent indeces.

Substituting Eq. (A8) into Eqs (A5) and (A6), we obtain

$$I_\parallel = \langle \sum_{g_1} \sum_{g_2} \Phi_{Zz}^2 \, \Phi_{Zg_1} \, \Phi_{Zg_2} \, \Phi_{g_1 q} \, \Phi_{g_2 q} \rangle \tag{A9}$$

and

$$I_\perp = \langle \sum_{g_1} \sum_{g_2} \Phi_{Zz}^2 \, \Phi_{Xg_1} \, \Phi_{Xg_2} \, \Phi_{g_1 q} \, \Phi_{g_2 q} \rangle. \tag{A10}$$

To change these equations into usable forms, note that averages are over the initial orientations of the molecule, meaning factors such as $\Phi_{g_1 q}$ and $\Phi_{g_2 q}$ are pulled out of the average sign (but left in the sum). Formally, Eq. (A9) is rewritten as

$$I_\parallel = \langle \sum_{g_1} \sum_{g_2} \Phi_{Zz}^2 \, \Phi_{Zg_1} \, \Phi_{Zg_2} \rangle \, \Phi_{g_1 q} \, \Phi_{g_2 q}, \tag{A11}$$

and Eq. (A10) can be rewritten in a similar fashion. Zare has shown[20] that the only nonvanishing terms occur when $g_1 = g_2$. Following Ref. 11a,

$$I_{\parallel} = \left\langle \frac{1}{15}\,\Phi_{xq}^2 + \frac{1}{15}\,\Phi_{yq}^2 + \frac{3}{15}\,\Phi_{zq}^2 \right.$$

$$= \left\langle \frac{1}{15}\,(\Phi_{xq}^2 + \Phi_{yq}^2 + \Phi_{zq}^2) + \frac{2}{15}\,\Phi_{zq}^2 \right\rangle$$

$$= \frac{1}{15} + \frac{2}{15}\,\langle \Phi_{zq}^2 \rangle\,, \tag{A12}$$

where use has been made of the identity

$$\sum_g \Phi_{gq}^2 = 1.$$

Similarly,

$$I_{\perp} = \frac{2}{15} - \frac{1}{15}\,\langle \Phi_{zq}^2 \rangle. \tag{A13}$$

At this point, we note that

$$\langle \Phi_{zq}^2 \rangle = \langle \cos^2\gamma \rangle, \tag{A14}$$

where γ is the angle between μ_{abs} and μ_{fl}. (This is really just the definition of $\langle \Phi_{zq}^2 \rangle$.) Substituting Eq. (A14) into Equations (A12) and (A13), and using the definition given by Eq. (4) the desired result is obtained.

$$P_{fl} = \frac{3\langle \cos^2\gamma \rangle - 1}{\langle \cos^2\gamma \rangle + 3}\,. \tag{A1}$$

Table 1. Polarization Values at Various Resonance Wavelengths

λ_{ex}(Å)	P_{fl}(x 10^2)	γ(degrees)
1698	-0.26	54.9
1575	2.66	52.9
1464	8.23	49.2
1402	4.07	52.0
1400	5.47	51.0
1394	6.40	50.4
1387	7.53	49.6
1331	0.09	54.6
1247	-0.08	54.7
1149	3.03	52.6

References for Chapter 5

1) W. M. Gelbart, Ann. Rev. Phys. Chem. 28, 323 (1977).

2) R. J. Van Brunt and R. N. Zare, J. Chem. Phys. 48, 4304 (1968).

3) J. Solomon, J. Chem. Phys. 47, 889 (1967).

4) a) J. H. Ling and K. R. Wilson, J. Chem. Phys. 65, 881 (1976).

b) M. Kawasaki, S. J. Lee, and R. Bersohn, J. Chem. Phys. 63, 809 (1975).

5) M. McClintock, W. Demtröder, and R. N. Zare, J. Chem. Phys. 51, 5509 (1969).

6) M. N. R. Ashfold and J. P. Simons, J. Chem. Soc. Faraday Trans. II 73, 858 (1977).

7) A. P. Baronavski and J. R. McDonald, Chem. Phys. Lett. 45, 172 (1977).

8) a) M. D. Morse, K. F. Freed, and Y. B. Band, Chem. Phys. Lett. 44, 125 (1976).

b) M. D. Morse, K. F. Freed, and Y. B. Band, J. Chem. Phys. 70, 3604 (1979).

c) M. D. Morse, K. F. Freed, and Y. B. Band, J. Chem. Phys. 70, 3620 (1979).

9) See Reference 15, Chapter 1 (this thesis).

10) a) Classical descriptions are frequently suitable for systems involving large J values (a consequence of the correspondence principle between classical and quantum mechanics). The ICN case produces fragments with large J values as discussed in Refs. (10b), (6), and (7).

b) A. Mele and H. Okabe, J. Chem. Phys. 51, 4798 (1969).

11) M. T. Macpherson, J. P. Simons, and R. N. Zare, Mol. Phys., in press.

12) Collisional depolarization has been discussed in R. G. Gordon, J. Chem. Phys. 45, 1643 (1966).

13) R. J. Spindler, J. Quant. Spectrosc. Radiat. Transfer 5, 165 (1965).

14) The same argument has been used for atomic quenching vs atomic depolarization in A. C. G. Mitchell and M. W. Zemansky, Resonance Radiation and Excited Atoms (Cambridge University Press, Cambridge, England, 1934).

15) The collisional quenching rate of $CN^*(B^2\Sigma^+)$ by ICN was discussed in the last chapter. The collisional quenching cross-section has been found to be independent of translational energy with a value of ~44 A^2 (quite large) by W. M. Jackson and J. L. Faris, J. Chem. Phys. 56, 95 (1972).

16) P. E. Zinsli, J. Phys. E 11, 17 (1978).

17) See Table 1 of Reference 11.

18) The transformation uses the conventions given by A. R. Edmonds, Angular Momentum in Quantum Mechanics. (Princeton University Press, Princeton, NJ, 1957).

19) R. N. Zare, J. Chem. Phys. 45, 4510 (1966).

20) R. N. Zare, private communication.

Figure Captions

Figure 1. Schematic diagram of the experimental setup.

Figure 2. Fluorescence decay curves of the polarized emission (background subtracted). The horizontal bar indicates the time period in which data were analyzed (see text).

Figure 3. Degree of polarization and fluorescent intensity of the CN fragment as a function of excitation wavelength. (Fluorescence excitation spectrum is uncorrected for variations of incident photon flux with wavelength; this does not affect the polarization measurements.)

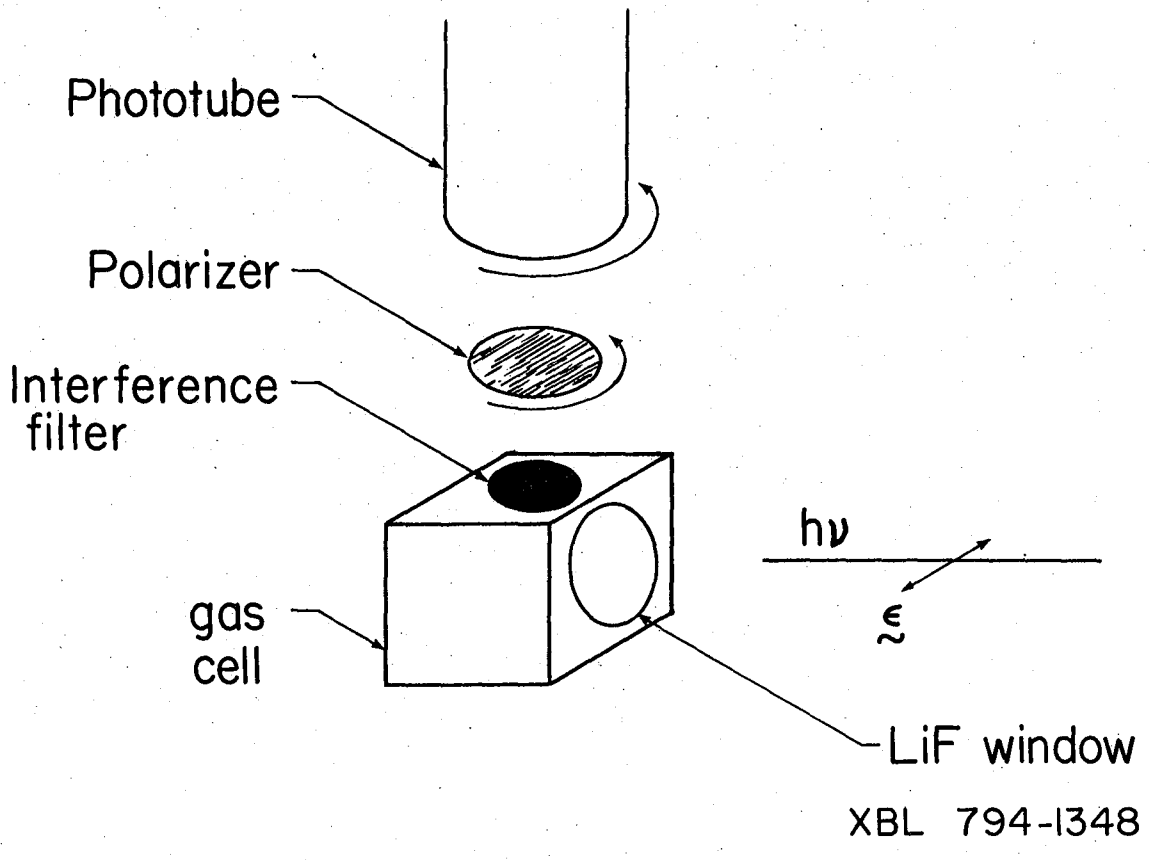
Phototube
Polarizer
Interference filter
gas cell
hν
ε
LiF window
XBL 794-1348

Figure 1

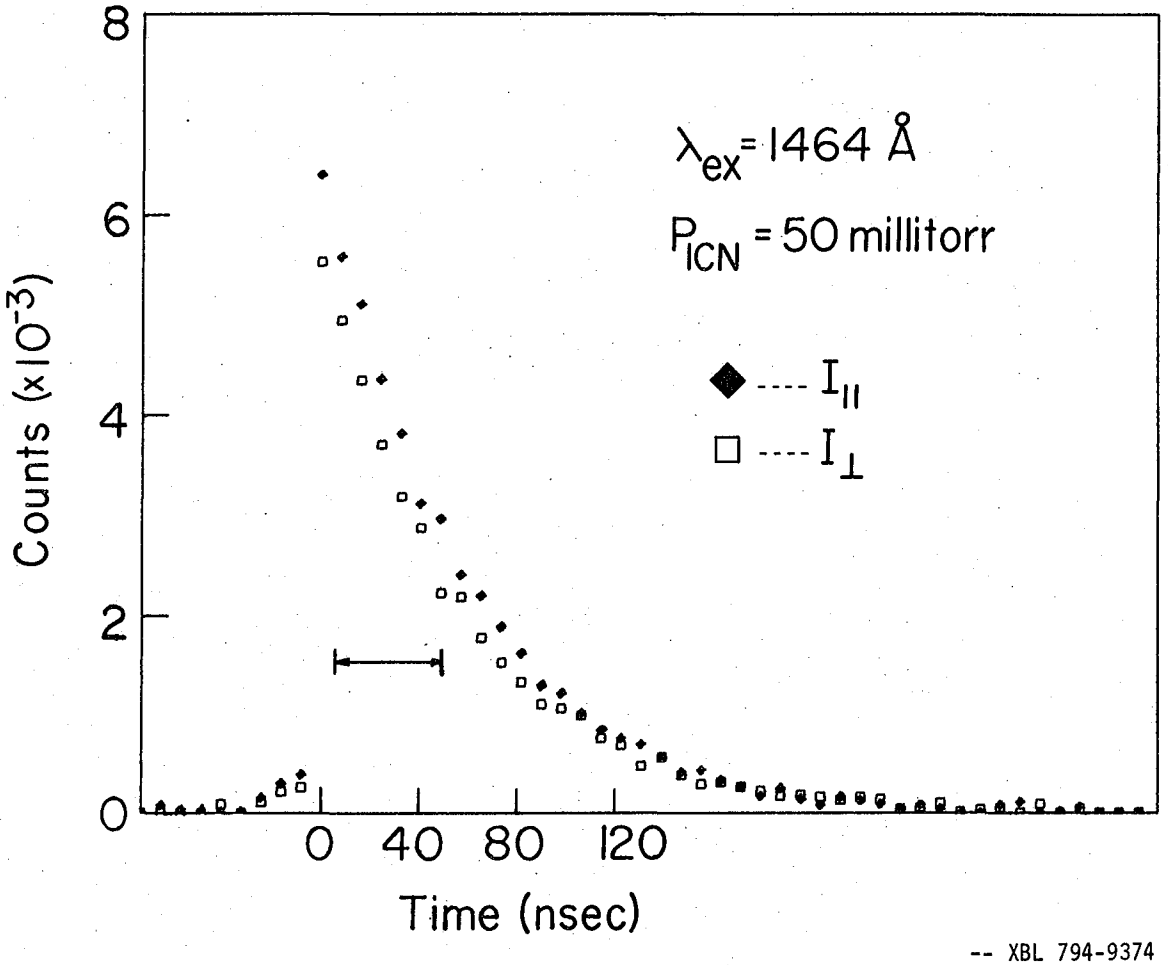

-- XBL 794-9374

Figure 2

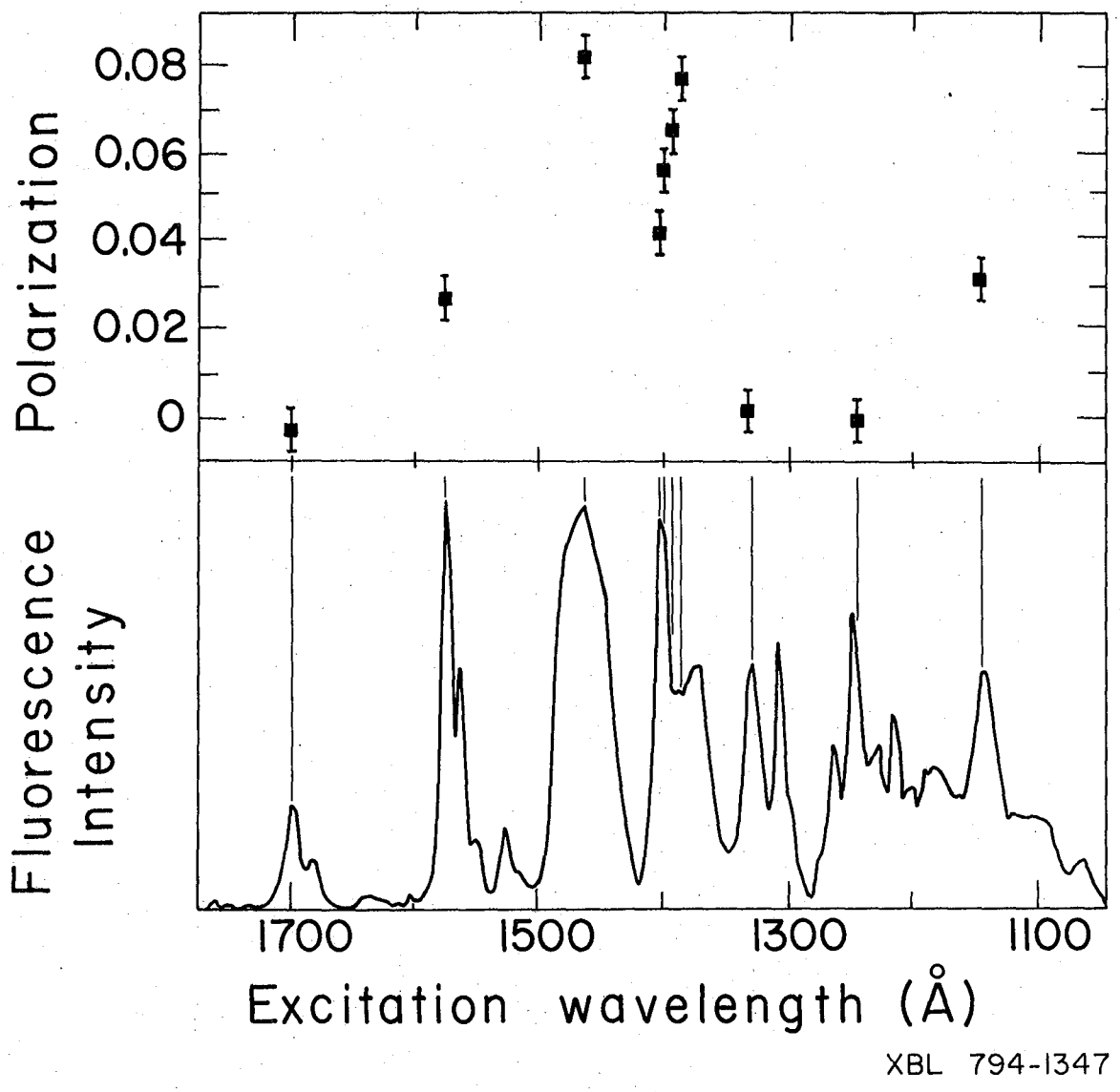
0.08
0.06
0.04
0.02
0
Polarization
Fluorescence Intensity
1700
1500
1300
1100
Excitation wavelength (Å)
XBL 794-1347

Figure 3

Chapter 6

Conclusions

It has been shown that the capabilities of synchrotron radiation are both diverse and promising. The timing and polarization properties have proved extremely useful for gas-phase VUV studies below 11.8 eV (the lithium fluoride cutoff energy). Time-of-flight (TOF) photoelectron spectroscopy of gases has also shown great promise at higher photon energies.[1]

This thesis is by no means exhaustive or comprehensive; rather, it gives a glimpse of possibilities the future holds. Attempting a broad view of any growing experimental technique is usually self-indulgent instead of visionary, but a few ideas are proposed anyway.

The polarization method described in the last chapter could also be applied to the photoionization process. In this case, one would be sensitive to the alignment of the molecular ion produced in the photoionization process. Preliminary studies by Caldwell and Zare[2] using a HeI resonance lamp have already demonstrated the feasibility of such experiments.

A considerably refined version of the monochromatized fluorescence apparatus described in Chapter 3 could be applied to study vibronic distributions of fragments populated by either photodissociation or photoionization. Again, resonance lamp studies have shown the feasibility of such projects[3] (for the photodissociation case), but little has been done with synchrotron radiation to exploit the many existing possibilities.

One particularly appealing experiment would utilize the tunability to study effects of resonance excitation (e.g., the Rydberg transitions of ICN) on state distributions of the products through monochromatized fluorescence measurements. Perhaps such measurements will be done in the future.

Technical progress also facilitates scientific progress. A "windowless" differentially-pumped branch line is currently under design for use at SSRL. The photon energy range will be $5\ eV \leq h\nu \leq 160\ eV$. I am waiting with bated breath...

All things considered, the scientific promise of synchrotron radiation for gas-phase research in physical chemistry is tremendous. A small fraction of this potential has been realized and discussed in this thesis. The most natural corollary to this conclusion is that there is a large fraction left to our collective imagination.

References for Chapter 6

1) a) M. G. White, R. A. Rosenberg, G. Gabor, E. D. Poliakoff, G. Thornton, S. H. Southworth, and D. A. Shirley, Rev. Sci. Instrument, 50, 0053 (1979).

b) M. G. White, Ph.D. Thesis, University of California at Berkeley, unpublished (1979).

c) R. A. Rosenberg, Ph.D. Thesis, University of California at Berkeley, unpublished (1979).

2) C. D. Caldwell and R. N. Zare, Phys. Rev. A 16, 255 (1977).

3) A. Mele and H. Okabe, J. Chem. Phys. 51, 4798 (1969).